UNIVERSIDADE DE SÃO PAULO
ESCOLA DE ENGENHARIA DE SÃO CARLOS

João Pedro Bozello Drudi

Piezoelectric nonlinear energy sink modelling and simulation for a blade vibration control problem

São Carlos

2020

João Pedro Bozello Drudi

Piezoelectric nonlinear energy sink modelling and simulation for a blade vibration control problem

Monografia apresentada ao Curso de Engenharia Mecânica, da Escola de Engenharia de São Carlos da Universidade de São Paulo, como parte dos requisitos para obtenção do título de Engenheiro Mecânico.

Supervisor: Prof. Dr. Paulo Celso Greco Júnior

São Carlos

2020

Catalog card prepared by Patron Service at "Prof. Dr. Sergio Rodrigues Fontes" Library at EESC/USP

Drudi, João Pedro Bozello
D794p Piezoelectric nonlinear energy sink modelling and simulation for a blade vibration control problem / João Pedro Bozello Drudi ; Monograph directed by Paulo Celso Greco Júnior. -- São Carlos, 2020.

Monograph (Undergraduate Thesis)Undergraduate Program in Mechanical Engineering -- São Carlos School of Engineering, at University of São Paulo, 2020.

1. Vibration attenuation. 2. Blade. 3. Nonlinear energy sink. 4. Piezoelectricity. I. Title.

Elena Luzia Palloni Gonçalves – CRB 8/4464

FOLHA DE AVALIAÇÃO

Candidato: João Pedro Bozello Drudi

Título: Piezoelectric nonlinear energy sink modelling and simulation for a blade vibration control problem

Trabalho de Conclusão de Curso apresentado à Escola de Engenharia de São Carlos da Universidade de São Paulo Curso de Engenharia Mecânica.

BANCA EXAMINADORA

Professor Associado Paulo Celso Greco Júnior (Orientador)

Nota atribuída: 10,0 (Dez)

(assinatura)

Professor Titular Marcelo Areias Trindade

Nota atribuída: 10,0 (Dez)

(assinatura)

Professora Associada Maíra Martins da Silva

Nota atribuída: 10,0 (Dez)

(assinatura)

Média: 10,0 (Dez)

Resultado: Aprovado

Data: 02/12/2020.

Este trabalho tem condições de ser hospedado no Portal Digital da Biblioteca da EESC

SIM ☒ NÃO ☐ Visto do orientador

Dedico este trabalho à minha família,
em especial à Bruna, à minha mãe, à minha irmã e aos meus avós.
Tudo aquilo que eu faço é por vocês.

ACKNOWLEDGEMENTS

Registro aqui meus mais sinceros agradecimentos e votos de apreço à minha namorada e companheira, Bruna, por todo o carinho e apoio incondicionais e incessantes ao longo de toda a nossa jornada pessoal e acadêmica, e a toda a minha família, especialmente à Helen, à Marília, à Zoraide e ao Olindo, pelo amor, suporte e ensinamentos diários. Devo a vocês tudo aquilo que sou e tudo aquilo que sei.

Também agradeço aos meus mais queridos amigos - Daniel Kitagawa, Daniel Siriano, Eduardo Kitagawa, Lucas Kauan Bianchesi, Marcelo Ikarimoto e Maurício Mani Marinheiro - pela vivência diária, fraternidade, ensinamentos, conversas, dificuldades, estudos e pela família que nos tornamos.

Finalmente, agradeço à Universidade de São Paulo, à Escola de Engenharia de São Carlos, e a todos os professores do Departamento de Engenharia Mecânica por toda a infraestrutura, oportunidade de aprendizado, apoio acadêmico e ensino de qualidade mundial a nós proprocionados. Também agradeço ao meu orientador, professor Paulo Celso Greco Júnior, pela dedicação e atenção ao longo do desenvolvimento deste trabalho.

ABSTRACT

DRUDI, J.P.B. **Piezoelectric nonlinear energy sink modelling and simulation for a blade vibration control problem**. 2020. Monografia (Trabalho de Conclusão de Curso) - Escola de Engenharia de São Carlos, Universidade de São Paulo, São Carlos, 2020.

In this work, a notional nonlinear energy sink model is proposed as a possible vibration control tool and applied to a single degree of freedom blade model. The principles for the mechanical and piezoelectric parameters acquisition are laid out and exemplified for the system (blade and piezoelectric patch) considered. Simplified electromechanical models are established and, from them, the ballpark of resulting electrical parameters (shunt circuit) are obtained with the intent of maximizing attenuation. The final, complete system is assessed on its performance through brief simulations in the frequency and time domains. With the results obtained from the models and simulations regarding the discussed blade-NES system, general conclusions are drawn showing that the modelled and simulated system has been proven effective in achieving vibration attenuation, at least theoretically, through a range of natural frequencies for the studied blade model. Finally, guidelines and general ideas for the next steps leading to a future experimental implementation are proposed and discussed, mainly regarding modelling techniques, literature, experimental parameters acquisition and practical feasibility concerns.

Keywords: Vibration attenuation. Blade. Nonlinear energy sink. Piezoelectricity.

RESUMO

DRUDI, J.P.B. **Piezoelectric nonlinear energy sink modelling and simulation for a blade vibration control problem**. 2020. Monografia (Trabalho de Conclusão de Curso) - Escola de Engenharia de São Carlos, Universidade de São Paulo, São Carlos, 2020.

Neste trabalho, um modelo hipotético de *nonlinear energy sink* é proposto como possível ferramenta de atenuação de vibração aplicada a um modelo de pá de um grau de liberdade. Os princípios para a aquisição dos parâmetros mecânicos e elétricos são mostrados e exemplificados para o sistema considerado (pá e pastilha piezoelétrica). Modelos eletromecânicos simplificados são estabelecidos e, a partir deles, valores aproximados dos parâmetros elétricos resultantes (circuito associado) são obtidos de maneira a maximizar o controle de vibração. O sistema final e completo é aferido por sua performance através de breves simulações nos domínios do tempo e da frequência. Com os resultados obtidos a partir dos modelos e simulações referentes ao sistema Pá-NES, conclusões gerais são traçadas mostrando que o sistema modelado e simulado se mostra eficaz na atenuação da vibração, ao menos teoricamente, por uma gama de frequências naturais para o modelo da pá estudada. Finalmente, ideias e linhas gerais para os próximos passos visando futuras implementações experimentais são propostas e discutidas, em especial no que se refere a técnicas de modelagem e sua respectiva literatura, aquisição experimental de parâmetros, e questões de viabilidade prática.

Palavras-chave: Controle de vibrações. Pá. Nonlinear energy sink. Piezoeletricidade.

LIST OF FIGURES

Figure 1 – Blade CAD (Autodesk Fusion 360) model. Front view on the left and Top view on the right. 20
Figure 2 – Single degree-of-freedom system representation 22
Figure 3 – Damping influence on the free response of SDOF systems. 24
Figure 4 – Frequency response (left) and Bode (right) plots. 25
Figure 5 – Cantilever plate representation. 31
Figure 6 – Tetrahedron lattice structure before (left) and after (right) mechanical strain 37
Figure 7 – 3-1 operation mode 39
Figure 8 – SDOF system with piezoelectric and shunt circuit attachment 42
Figure 9 – Representation of a shunt circuit with a nonlinear element. 44
Figure 10 – Blade CAD model render and views 52
Figure 11 – Example of sample measurements on the blade model 52
Figure 12 – Blade mesh before and after the PATRAN/Nastran solver run 54
Figure 13 – Nodes selected to represent the piezoelectric patch position 57
Figure 14 – Notional example of nodes before (top) and after (bottom) deformation 57
Figure 15 – Data sheet information (Midé QP10N) 60
Figure 16 – Fundamental frequency response 66
Figure 17 – Second to Fifth natural frequencies response 67
Figure 18 – Free vibration time response, fundamental frequency 69
Figure 19 – Free vibration time response, Second to Fifth natural frequencies . . . 69
Figure 20 – Base excitation time response at the fundamental frequency 70
Figure 21 – Base excitation time response, Second to Fifth natural frequencies . . . 71

LIST OF TABLES

Table 1 – Plate geometry and mechanical properties 52
Table 2 – Approximate plate eigenvalues ($\nu = 0.33$) (INOYAMA, 2003) 53
Table 3 – Approximate natural frequencies ($\nu = 0.33$, $L/w = 2.12$) 53
Table 4 – FEM Simulation Parameters 54
Table 5 – FEM Simulation Results (PATRAN) 54
Table 6 – FEM Simulation Results (Fusion 360) 55
Table 7 – Generalized mass and stiffness values 56
Table 8 – Distances and elongation of relevant nodes 58
Table 9 – PZT-5A physical properties 59
Table 10 – Theoretical approximation to the piezoelectric constants 60
Table 11 – PZT-5A patch - resulting constants, equation 2.58 62
Table 12 – Ballpark of optimal electric parameters obtained 65

CONTENTS

1 INTRODUCTION 19

2 THEORY AND LITERATURE REVIEW 21
2.1 Classical Mechanics and Vibrations 21
2.2 Single degree-of-freedom systems 22
2.2.1 The Single-degree-of-freedom model and its homogeneous solution 22
2.2.2 Frequency analysis of SDOF systems and harmonic excitations 23
2.2.3 The solution of SDOF systems under general excitations 25
2.2.4 Transfer functions of SDOF systems 26
2.3 Several degrees-of-freedom and continuous systems 26
2.3.1 The Multi-degrees-of-freedom model 26
2.3.1.1 Modal analysis of a MDOF system 27
2.3.1.2 Solutions and modal analysis of a MDOF system in state-space form 29
2.3.2 Continuous systems 30
2.3.2.1 The plate vibration case 30
2.3.3 Numerical solutions using the Finite Element Method 32
2.3.3.1 Eigenvalue extraction 33
2.3.3.2 Normalization of eigenvectors 34
2.4 Experimental vibration 35
2.4.1 Dealing with damping 35
2.5 Piezoelectric theory 36
2.5.1 3-1 operation mode 38
2.5.2 Single degree of freedom model 39
2.5.3 Higher order models 41
2.5.4 Piezoelectric applications to vibration control 41
2.5.5 Nonlinear energy sinks 43
2.5.6 Piezoelectric transducer localization 45

3 MODELLING AND SIMULATION DEVELOPMENT 47
3.1 Blade and blade-NES models 47
3.1.1 Single-degree-of-freedom model 47
3.1.2 SDOF transfer functions, general forcing 48
3.1.3 SDOF transfer functions, base excitation and inertial excitation 50
3.2 Mechanical parameters 51
3.2.1 Blade modal analysis: plate approximation quasi-analytical solutions 51
3.2.2 Blade modal analysis: PATRAN-Nastran numerical solutions 53

3.2.3 Blade modal analysis: Fusion 360 numerical solutions . . . 54
3.2.4 Mass and stiffness parameters . . . 55
3.2.5 Correction of the single-degree-of-freedom model . . . 56
3.3 Piezoelectric parameters . . . 59
3.3.1 Theoretical approximation approach . . . 59
3.3.2 Datasheet approach . . . 60
3.3.3 Experimental approach . . . 62
3.4 Electrical parameters . . . 62
3.4.1 Python script for finding the optimal electrical-domain parameters . . . 63
3.5 Frequency-domain response solutions . . . 65
3.6 Time-domain response solutions . . . 67
3.6.1 Free response damping performance . . . 67
3.6.2 Base motion damping performance . . . 69

4 CONCLUSION AND FURTHER DEVELOPMENTS . . . 73
4.1 Conclusions on the simulation results . . . 73
4.2 Proposed improvements and further developments . . . 74
4.2.1 Development of higher order models for the system . . . 74
4.2.2 Future experimental procedures . . . 75

BIBLIOGRAPHY . . . 77

1 INTRODUCTION

A broad spectrum of engineering applications relies on the control of vibrating structures. When dealing with the forced vibration of bladed disks, the understanding of the system's aerodynamics, mode localization and damping is of paramount importance (SLATER; MINKIEWICZ; BLAIR, 1999). The current industry-standard state of turbomachinery design and manufacturing, aiming aerodynamic efficiency and weight reduction, has not only allowed for those advances to take place but has also contributed to diminished intrinsic damping of blades (KAUFFMAN; LESIEUTRE, 2012), what possibly results in distinct noise, vibration and harshness problems such as high-cycle fatigue and subsequent lifetime reduction, and comfort reduction.

Regarding its modes of vibration, the dynamics of the rotating assembly has to be taken into consideration, and such behaviour can have different properties depending on the symmetry achieved in its geometry. A perfectly symmetrical bladed disk (also known as the tuned case) will have a large number of repeated natural frequencies and periodic corresponding mode shapes, while an asymmetrical assembly (mistuned or detuned) will have an ample and continuous spectrum of natural frequencies (SLATER; MINKIEWICZ; BLAIR, 1999) which change due to being subjected to high centrifugal loads and changing rotational speeds (KAUFFMAN; LESIEUTRE, 2012). This of course serves as a motivation for the application of broadband vibration attenuation (SILVA et al., 2018; ZHOU; THOUVEREZ; LENOIR, 2014a; ZHOU; THOUVEREZ; LENOIR, 2014b), as will be discussed later. It should be understood that the mistuning of bladed disks, although generally small (e.g. on the order of 10% or less of nominal natural frequency values), can drastically increase internal stresses and strains, possibly leading to premature high cycle fatigue (CASTANIER; PIERRE, 2006), what by itself motivates the study of control techniques for such problems.

A non-symmetrical blisk is said to be detuned when its asymmetries originate from intentional parameter variations (e.g. alternation of types of blades, design geometry specifications, etc), whereas a mistuned blisk is one where such asymmetries derive from random or unpredictable phenomena (e.g. manufacturing and materials, wear, etc) (STERNCHÜSS, 2009). Those discerning definitions notwithstanding, such non-symmetrical systems will hereinafter be treated alike and no geometrical periodicity will be attributed to the systems described, as the focus of the discussions and simulations presented will always be on the vibration of the blade itself.

For the appropriate treatment of the vibration control methods provided by the literature and of the ones chosen for the applications here discussed, it's essential to make use of proper modelling techniques and methods, a seen in sections two and three. This

fundamental element of the analysis proposed was studied by computational approaches which rely on the geometric modelling of the blade provided by its CAD (Computer Aided Design) structure. Figure 1 below shows the representation of the blade as used here. Based on it, simulations regarding its vibration behaviour, modal strains, and natural frequencies will be developed, laying the groundwork for the vibration damping assessments which constitute the core of this work.

Figure 1 – Blade CAD (Autodesk Fusion 360) model. Front view on the left and Top view on the right.

Several methods to mitigate vibration in bladed disks have been studied since the 1980's, usually making use of additional damping introduced into the structure, and more recently a trend towards the implementation of piezoelectrics can be observed, mainly because of its light weight, high bandwidths, efficient energy conversion, and easy integration (JALILI, 2009; ZHOU; THOUVEREZ; LENOIR, 2014a). Among the many possible applications of piezoelectric circuits to the vibration control problem (ERTURK; INMAN, 2011; GRIPP; RADE, 2018; JALILI, 2009), the use of *Nonlinear energy sinks* will be discussed due to the effectiveness of its applications in problems similar to the blade vibration attenuation so far proposed.

Precisely, the intent of this work is to discuss, model, simulate and assess the damping performance of a cubic voltage-charge behaviour nonlinear energy sink (SILVA et al., 2018) to a single vibrating blade as a precursory step towards the same implementation on full bladed disk assemblies.

Due to the limited experimental conditions imposed by the current Brazilian (and worldwide) public health scenario, the development will waive the experimental approach and procedures and instead focus on the modelling and simulation of the vibration problem proposed, as a way to provide the groundwork for future applications in this realm.

2 THEORY AND LITERATURE REVIEW

2.1 Classical Mechanics and Vibrations

The theoretical basis of this work is started by providing a quick reminder of some fruitful results from classical mechanics which will be used throughout the provided literature – yet here the development itself won't necessarily include them, but rather their results as derived and implemented by the references.

From the most general principle of dynamics, that being *Hamilton's Principle*, we can state (LANDAU; LIFSHITZ, 2013a, p. 2):

$$\delta S = \delta \int_{t_1}^{t_2} L(q, \dot{q}, t) dt = 0 \tag{2.1}$$

Where the *Lagragian* L, a function of the generalized coordinates $\{q\}$ and their derivatives $\{\dot{q}\}$, is usually defined for purely mechanical systems as the difference between the kinetic energy T and the potential energy U for the system and its elements (LANDAU; LIFSHITZ, 2013a, p. 6). The statement of Equation 2.1 above is of course analogous to the use of the *Euler-Lagrange equations* in each generalized coordinate q_k for the same system and elements (LANDAU; LIFSHITZ, 2013a, p. 3):

$$\frac{\mathrm{d}}{\mathrm{d}t}\left(\frac{\partial L}{\partial \dot{q}_i}\right) - \frac{\partial L}{\partial q_i} = 0 \tag{2.2}$$

A different formulation of this principle, usually more useful for dealing with continuous systems under the influence of external excitations, is expressed below and known as the *Extended Hamilton's principle* (JALILI, 2009):

$$\int_{t_1}^{t_2} (\delta L(q, \dot{q}, t) + \delta W^{ext}) dt = \int_{t_1}^{t_2} (\delta W^{ext} + \delta T - \delta U) = 0 \tag{2.3}$$

This of course takes into account both conservative (in the form of the potential U) and non-conservative forces (under the external work W^{ext}) acting in or on the system (JALILI, 2009).

The application of the Euler-Lagrange equations for a Lagrangian of the form:

$$L(\{x\}, \{v\}) = \sum_i \frac{1}{2} m_i v_i^2 - U(\{\mathbf{r}_i\}) \tag{2.4}$$

Results in equations of motion of the following form (LANDAU; LIFSHITZ, 2013a, p. 9), for each body:

$$m_i \dot{\mathbf{v}}_i = -\frac{\partial U}{\partial \mathbf{r}_i} = \mathbf{F}_i \tag{2.5}$$

What is referred to as *Newton's second law*, which proves to be most useful in the applications where it's reasonable to assume lumped-parameters, and the generalized coordinates can readily be expressed in cartesian (or otherwise) vector form.

With those tools laid out, the discussion can now focus on the applications of vibrations to the specific types of system which best represent the problems proposed so far.

2.2 Single degree-of-freedom systems

By the use of the fundamental principles of dynamics stated above on the modelling of oscillating systems, it's possible to infer, under a set of assumptions and hypotheses regarding the system and its elements, about its behaviour in time during (forced case) or after (free-vibration case) the application of loads and excitations.

2.2.1 The Single-degree-of-freedom model and its homogeneous solution

Starting with the simplest assumptions for a system, we can propose a single degree-of-freedom (SDOF) model as illustrated by Figure 2.

Figure 2 – Single degree-of-freedom system representation

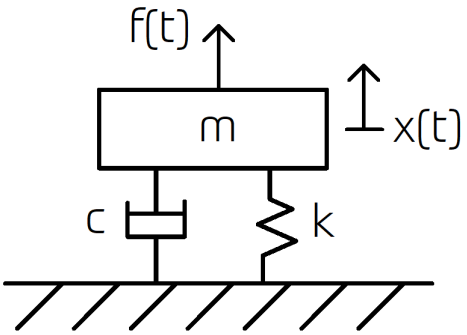

With the usual elastic element and viscous-damping element models as provided by the literature (CRAIG Jr; KURDILA, 2006; RAO, 2017), we can apply Newton's second law to the mass to obtain the differential equation that describes its motion in the coordinate x under forced conditions with equation 2.6 (CRAIG Jr; KURDILA, 2006):

$$m\ddot{x} + c\dot{x} + kx = f(t) \tag{2.6}$$

Where f(t) is a general excitation in the x coordinate, and the case f(t) = 0 provides the free response for the system (CRAIG Jr; KURDILA, 2006), which will then behave according to its initial conditions for x and $\ddot{x}$ (LANDAU; LIFSHITZ, 2013a, p. 59). We can, of course, rewrite equation 2.6 in the form of equation 2.7 (CRAIG Jr; KURDILA, 2006):

$$\ddot{x} + 2\zeta\omega_n\ddot{x} + \omega_n^2 x = \frac{\omega_n^2}{k} f(t) \tag{2.7}$$

Where:

$$\omega_n = \sqrt{\frac{k}{m}} \qquad \zeta = \frac{c}{2m\omega_n}$$

The parameters ζ and ω_n are, respectively, the *viscous damping factor* and the *undamped natural frequency* (CRAIG Jr; KURDILA, 2006) of the system. Considering again the free-response (f(t) = 0) case, the general solution for equation 2.7 is equation 2.8 below (RAO, 2017):

$$x_h(t) = C_1 e^{\{\zeta + \sqrt{\zeta^2 - 1}\}\omega_n t} + C_2 e^{\{\zeta - \sqrt{\zeta^2 - 1}\}\omega_n t} \tag{2.8}$$

Where C_1 and C_2 are constants which depend only on the initial conditions of the system, what brings the conclusion that the free-response of a SDOF system depends only on its initial conditions and intrinsic parameters m, c and k, and the even more specific case where c = ζ = 0 leads to the free undamped vibration of the mass m in the coordinate x (RAO, 2017). The presence of a non-zero damping in the model of the system, however, dictates its cyclic behaviour once under free-vibration conditions, as is clear by the presence of factors of ζ in the exponential solution above (equation 2.8) (LANDAU; LIFSHITZ, 2013a, p. 75). This gives rise to the comparison between overdamped ($\zeta > 1$), critically damped ($\zeta = 1$) and underdamped ($0 < \zeta < 1$) systems as illustrated below by figure 3 (RAO, 2017):

Now if it's assumed that the system behaves as a SDOF model, from the time-domain response as above we can work our way back to the parameters of the differential equation of the system, equation 2.6, by the use of some experimental procedures (CRAIG Jr; KURDILA, 2006; RAO, 2017). The experimental determination of vibration parameters will be the subject of later sections.

2.2.2 Frequency analysis of SDOF systems and harmonic excitations

Now going back to the more general forced case, the particular solution to the differential equation 2.6 will depend, of course, on the form f(t) takes (LANDAU; LIFSHITZ,

Figure 3 – Damping influence on the free response of SDOF systems.

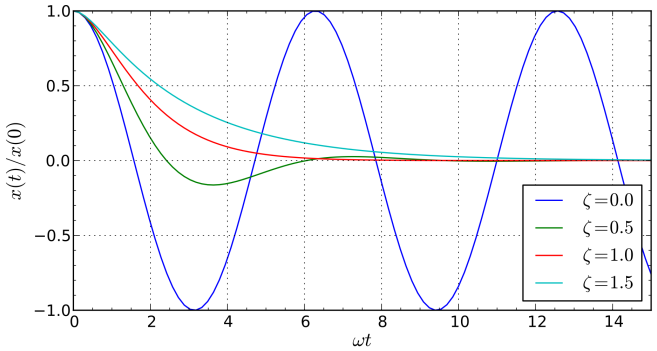

Source: Wikipedia, 10/30/2020

2013a, p. 61). Before generalizing f(t), let's first consider the harmonic case, where f(t) takes the form (CRAIG Jr; KURDILA, 2006, p. 87):

$$f(t) = f_0\, cos(\Omega t) \tag{2.9}$$

This consideration is especially fruitful once experimental frequency response methods are taken into consideration, as will be discussed later, but some results can be clearly observed through the conclusion that the particular steady-state solution $x_p(t)$ will behave analogously (CRAIG Jr; KURDILA, 2006, p. 87):

$$x_p(t) = X cos(\Omega t - \alpha) \tag{2.10}$$

If we consider the behaviour of the solution through the spectrum of possible forcing frequencies Ω, we arrive at the *frequency response* (CRAIG Jr; KURDILA, 2006, p. 88) of the system, which is characterized by a *steady-state magnification factor* D_s and a *phase angle* α. The expressions for those are:

$$D_s(r) = \frac{X(r)}{X_0} = \frac{1}{\sqrt{(1-r^2)^2 + (2\zeta r)^2}} \quad , \qquad tan[\alpha(r)] = \frac{2\zeta r}{1-r^2} \tag{2.11}$$

Where $r = \frac{\Omega}{\omega_n}$ is the *normalized frequency* and $X_0 = \frac{f_0}{k}$ is the *static displacement*. The plots in figure 4 – called *frequency response plots* or, when adjusted to a logarithmic scale, *bode plots* – display how phase and magnification change with the normalized frequency of excitation, for different values of ζ (CRAIG Jr; KURDILA, 2006, p. 89).

Finally, in this case the general solution for x(t) is, of course, the sum of the homogeneous and particular solutions. Using the homogenous solution as before, the total response for a harmonically excited SDOF mechanical system is as below (CRAIG Jr; KURDILA, 2006, p. 90):

Figure 4 – Frequency response (left) and Bode (right) plots.

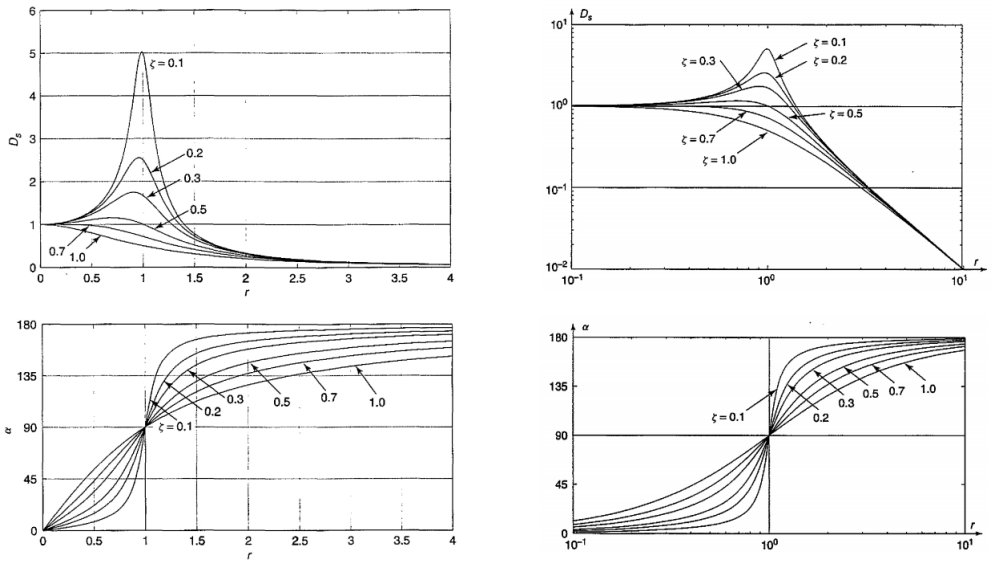

Source: (CRAIG Jr; KURDILA, 2006, p. 89)

$$x(t) = x_h(t) + x_p(t)$$
$$= \frac{X_0}{\sqrt{(1-r^2)^2 + (2\zeta r)^2}} cos(\Omega t - \alpha) \; + \; C_1 e^{\{\zeta + \sqrt{\zeta^2 - 1}\}\omega_n t} \; + \; C_2 e^{\{\zeta - \sqrt{\zeta^2 - 1}\}\omega_n t}$$

2.2.3 The solution of SDOF systems under general excitations

Now back at the most general forcing case, if the system is linear – and hence the principle of superposition holds (CRAIG Jr; KURDILA, 2006, p. 171) – and it has initial conditions equal to zero for both position and speed, we can make use of a *Convolution* to obtain the total response for any f(t) (CRAIG Jr; KURDILA, 2006, p. 126) (RAO, 2017, p. 426):

$$x(t) = (f * g)(t) \tag{2.12}$$

Where the function g(t) is of the form:

$$g(t) = \frac{1}{m\omega_n \sqrt{1-\zeta^2}} \, e^{-\zeta\omega_n t} \, sin(\omega_n \sqrt{1-\zeta^2}\, t) \tag{2.13}$$

By remembering the definition of the *Convolution Integral*, we can arrive at the total response in the integral form:

$$x(t) = \int_0^t f(\tau) g(t-\tau) \, d\tau \tag{2.14}$$

2.2.4 Transfer functions of SDOF systems

Now let us apply the Laplace transform to the governing differential equation (equation 2.6), assuming zero initial conditions, and suppose we arrive at an algebraic equation in the form (CRAIG Jr; KURDILA, 2006, p. 138):

$$H_{m,c,k}(s)X(s) = H_f(s)F(s) \tag{2.15}$$

We can define the *impedance function* and the *transfer function*, respectively, as:

$$Z(s) = \frac{H_{m,c,k}(s)}{H_f(s)} \quad \Rightarrow \quad Z(s)X(s) = F(s) \tag{2.16}$$

$$H(s) = \frac{H_f(s)}{H_{m,c,k}(s)} \quad \Rightarrow \quad X(s) = H(s)F(s) \tag{2.17}$$

So now, taking the inverse Laplace transform of X(s), we may obtain the total response of the system through yet another approach, from the right-hand side of equation 2.17 above:

$$x(t) = \mathcal{L}^{-1}[H(s)F(s)] \tag{2.18}$$

2.3 Several degrees-of-freedom and continuous systems

Let us now consider the problem of finding the equations of motion (and later their solutions) for a continuous system. The modelling of such systems invariably leads to the obtention of partial differential equations (CRAIG Jr; KURDILA, 2006, p. 367), and finding their solutions might range from difficult to analytically impossible (RAO, 2017, p. 598). Continuous systems might, then, be approximated as discrete MDOF systems, which as will be seen produce a set of ordinary differential equations, what in place can be straightforward to solve either analytically or numerically.

2.3.1 The Multi-degrees-of-freedom model

Whether we are dealing with a truly enough discrete multibody system or approximating a continuous system as a n-degrees-of-freedom system, the application of Newton's law or Lagrange's equations to each of a set $\{q_n\}$ of n generalized coordinates is going to provide us a set of n equations (LANDAU; LIFSHITZ, 2013a, p. 66), linear or otherwise, whose solutions deliver the total response of the system under consideration under the limitations of the hypotheses assumed. If the system can be approximated by a pattern of

masses, springs and dampers as formerly described, this set of equations can be expressed in the matrix form below (RAO, 2007, p. 43):

$$[M]\ddot{\mathbf{x}} + [C]\dot{\mathbf{x}} + [K]\mathbf{x} = \mathbf{f} \tag{2.19}$$

Where [M], [C] and [K] are respectively the mass, damping and stiffness matrices, and the vectors $\ddot{\mathbf{x}}$, $\dot{\mathbf{x}}$, $\mathbf{x}$ and $\mathbf{f}$ are the acceleration, velocities, displacements and force vectors. The matrices are, of course, according to the *Betti-Maxwell reciprocity theorem*, symmetric (SILVA, 2007, p. 4.5).

2.3.1.1 Modal analysis of a MDOF system

The set of coupled differential equations provided by equation 2.19 above can be decoupled by the Modal Analysis procedure (RAO, 2007, p. 45), requiring the determination of natural frequencies and normal modes for the system analogously to what was done for a SDOF system. Since natural frequencies are not affected by loading or damping conditions as seen in the SDOF case, let's take as a starting point the undamped free vibration of the system in case, described by:

$$[M]\ddot{\mathbf{x}} + [K]\mathbf{x} = \mathbf{0} \tag{2.20}$$

Assuming a general harmonic solution for each coordinate k (LANDAU; LIFSHITZ, 2013a, p. 67):

$$x_k(t) = X_k\, e^{i\omega t} \tag{2.21}$$

Our system reduces to:

$$([K] - \omega^2[M])\mathbf{X} = \mathbf{0} \tag{2.22}$$

Equation which represents a system of algebraic homogeneous equations for each X_k in $\mathbf{X}$ and will provide nontrivial solutions if and only if (RAO, 2007, p. 45):

$$det([K] - \omega^2[M]) = 0 \tag{2.23}$$

The equation above, called the *characteristic equation* of the system, has n real positive roots ω^2, some of which may or may not coincide, and the set $\{\omega_k\}$ of n positive ω values is called the *eigenfrequencies* or natural frequencies of the system (LANDAU; LIFSHITZ, 2013a, p. 67). This equation is, of course, an eigenvalue problem where associated to each eigenvalue ω^2 (and, correspondingly, to each natural frequency ω) there

is an eigenvector $\mathbf{X}$ called a *natural vibration mode* of the system (CRAIG Jr; KURDILA, 2006, p. 283). In specific, the set $\{\omega_k\}$ will naturally have a smallest value, which is usually represented by ω_1 and called the first natural frequency or *fundamental frequency*, to which there will be an associated $\mathbf{X}_1$ mode called the *fundamental mode* (RAO, 2007, p. 46).

It's important to notice that the set of eigenvectors $\{\mathbf{X}_k\}$ forms an n-dimensional orthogonal base (RAO, 2007, p. 46), or an orthonormal base once its elements are normalized (CRAIG Jr; KURDILA, 2006, p. 283) as will be discussed later. This property allows for the decoupling of the differential equations in equation 2.19 by the use of normal coordinates (LANDAU; LIFSHITZ, 2013a, p. 67) (CRAIG Jr; KURDILA, 2006, p. 293). Let us first define the modal matrix of the system:

$$\mathbf{\Phi} = [\mathbf{X_1} \dots \mathbf{X_n}] \tag{2.24}$$

Now let us define the normal coordinates as the set of generalised coordinates $\{\eta_k\}$ where the system executes in each η_k a simple periodic oscillation (LANDAU; LIFSHITZ, 2013a, p. 67), and, as such, satisfies (CRAIG Jr; KURDILA, 2006, p. 297):

$$\mathbf{x}(t) = \sum_{k=1}^{n} \phi_k \, \eta_k = \mathbf{\Phi} \cdot \eta(t) \tag{2.25}$$

Where η is the vector of the coordinates $\{\eta_k\}$. Then, by applying this solution to equation 2.19:

$$[M_m]\ddot{\eta} + [C_m]\dot{\eta} + [K_m]\eta = \mathbf{\Phi}^T \mathbf{f}(t) \tag{2.26}$$

Where the modal mass, generalized damping, and modal stiffness matrices are respectively defined by (CRAIG Jr; KURDILA, 2006, p. 297):

$$\begin{aligned} [M_m] &= \mathbf{\Phi}^T [M] \mathbf{\Phi} \\ [C_m] &= \mathbf{\Phi}^T [C] \mathbf{\Phi} \\ [K_m] &= \mathbf{\Phi}^T [K] \mathbf{\Phi} \end{aligned}$$

The last two equations, then, provide a method for arriving at an uncoupled set of equations. Those describe the same system as equation 2.19, but are considerably easier to solve analytically or numerically (RAO, 2007, p. 755) and can be used in the process of experimental modal analysis (SILVA, 2007, p. 4.3) as explained in later sections.

2.3.1.2 Solutions and modal analysis of a MDOF system in state-space form

Going back now to the original equation 2.19, we can rearrange it to find an expression for the acceleration vector (RAO, 2007, p. 54):

$$\ddot{\mathbf{x}}(t) = -[M]^{-1}[C]\dot{\mathbf{x}}(t) - [M]^{-1}[K]\mathbf{x}(t) + -[M]^{-1}\mathbf{f}(t) \tag{2.27}$$

Which can be represented in state-space form by:

$$\dot{\mathbf{y}}(t) = [A]\mathbf{y}(t) + [B]\mathbf{f}(t) \tag{2.28}$$

Where $\mathbf{y}(t)$ is the 2n-dimensional state vector:

$$\mathbf{y}(t) = \begin{Bmatrix} \mathbf{x}(t) \\ \dot{\mathbf{x}}(t) \end{Bmatrix} \tag{2.29}$$

And [A] and [B] are 2n x 2n matrices defined as:

$$[A] = \begin{bmatrix} [0]_n & [I]_n \\ -[M]^{-1}[K] & -[M]^{-1}[C] \end{bmatrix} \tag{2.30}$$

$$[B] = \begin{bmatrix} [0]_n \\ [M]^{-1} \end{bmatrix} \tag{2.31}$$

Now, through the same procedure used before for the system in configuration space form, letting $\mathbf{f}(t) = 0$ for the free-response of the system, the normal modes and natural frequencies might by obtained by finding the solution to two eigenvalue problems of the form (RAO, 2007, p. 54):

$$[A]\mathbf{Y} = \lambda\mathbf{Y} \tag{2.32}$$

And:

$$[A]^T\mathbf{Z} = \lambda\mathbf{Z} \tag{2.33}$$

Which will result in finding n complex (or otherwise) eigenvalues (and their respective natural frequencies) and their corresponding n right eigenvectors $\mathbf{Y}$ and n left eigenvectors $\mathbf{Z}$. And the state-space solution for $\mathbf{y}(t)$ will take the form (RAO, 2007, p. 57):

$$\mathbf{y}(t) = \int_0^t [Y]e^{[\lambda_i](t-\tau)}\mathbf{Q}(\tau)d\tau + [Y]e^{[\lambda_i]t}\eta(0) \tag{2.34}$$

Where $\mathbf{Q}(t)$ is the vector of modal forces defined by:

$$\mathbf{Q}(t) = [Z]^t[B]\mathbf{f}(t) \tag{2.35}$$

And $\eta(0)$ is the initial value of the 2n modal coordinates $\eta(t)$, which are assumed in the solution of the state equation:

$$\mathbf{y}(t) = \sum_{k=1}^{2n} \eta_k \mathbf{Y}^k = [Y]\ \eta(t) \tag{2.36}$$

And which can be obtained by:

$$\eta(t) = \int_0^t e^{[\lambda_i](t-\tau)}\mathbf{Q}(\tau)d\tau + e^{[\lambda_i]t}\eta(0) \tag{2.37}$$

Equations 2.32 and 2.33, then, provide the modal analysis using state-space form for the problem stated in configuration space by equation 2.20, while equation 2.34 provides its total response in the time domain.

2.3.2 Continuous systems

For a properly rigorous treatment of the modelling of continuous systems, the reader is encouraged to follow the literature regarding continuum mechanics and the theory of elasticity (LANDAU; LIFSHITZ, 2013b; TIMOSHENKO; GOODIER, 2011), while more specific works on their vibration behaviour (RAO, 2007) can provide the appropriate methods and techniques for time- and frequency-domain solutions (e.g. through modal analysis, integral transforms, numerical methods and quasi-analytical methods such as Rayleigh's, Rayleigh-Ritz and Garlekin's).

The development here, however, will be focused on one single problem which approximates closely enough our blade vibration case to be used both as a comparison and as a sanity check for the numerical solutions later achieved.

2.3.2.1 The plate vibration case

Let' consider then the case of a thin plate model as shown in figure 5 and analyse its vibration behaviour.

Using the *Kirchhoff model* of small deflections for the plate (RAO, 2007, p. 465) and the extended Hamilton's principle (equation 2.3), one can arrive at the following forced motion for the transverse (represented by the displacement coordinate $w(x, y, t)$) vibration of the plate considered (RAO, 2007, p. 468):

$$D\nabla^4 w + \rho h\ddot{w} = f \tag{2.38}$$

Figure 5 – Cantilever plate representation.

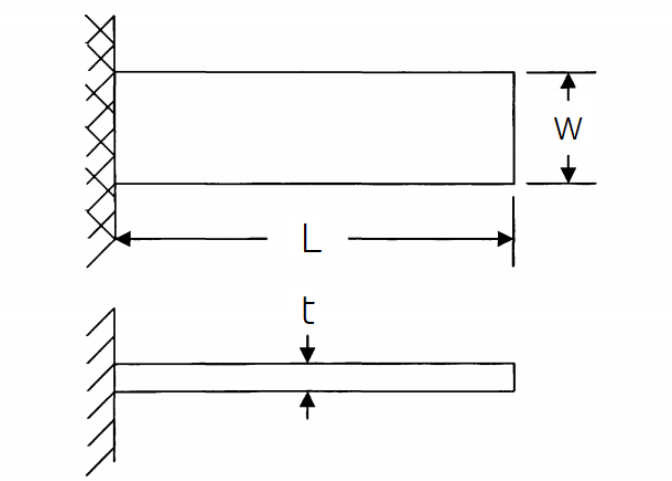

In which we consider a general force $f = f(x, y, t)$, and D and ∇^4 are respectively the *flexural rigidity* of the plate and the *biharmonic operator*, both defined as below (RAO, 2007, p. 466):

$$D = \frac{Eh^3}{12(1-\nu^2)}$$

$$\nabla^4 = \frac{\partial^4}{\partial x^4} + \frac{\partial^4}{\partial x^2 \partial y^2} + \frac{\partial^4}{\partial y^4}$$

Now, for finding the vibration modes associated with equation 2.38 we must make use of the plate's *boundary conditions* (natural and geometric) (RAO, 2007, p. 482), set the free vibration condition $f = 0$, and assume an harmonic solution, just as done before for the Single- and Multi-degrees-of-freedom cases:

$$w(x, y, t) = W(x, y)e^{i\omega t} \tag{2.39}$$

Which then reduces our problem to an eigenvalue equation of the form (RAO, 2007, p. 480):

$$\nabla^2 W - \lambda^4 W = 0 \tag{2.40}$$

Where, using the boundary conditions of a cantilever (CFFF) plate (INOYAMA, 2003):

$$\lambda^4 = \frac{\omega^2 a^4 \rho h}{D} \quad \Leftrightarrow \quad \lambda^2 = \omega a^2 \sqrt{\frac{\rho h}{D}} \tag{2.41}$$

So, for each eigenvalue λ_n found, we have an associated natural frequency:

$$\omega_n = \frac{\lambda_n^2}{a^2}\sqrt{\frac{Eh^2}{12\rho(1-\nu^2)}} \tag{2.42}$$

Considering that this eigenvalue problem does not have a closed form solution (INOYAMA, 2003), the natural frequencies ω_n must be numerically determined for a specific plate geometry, as will be exemplified later in section 3.

2.3.3 Numerical solutions using the Finite Element Method

Using the logic provided in the beginning of this section, the *Finite Element Method* (FEM) is the mathematical modelling of a continuous system as a MDOF system of discrete elements assumed to be interconnected at certain nodes, providing the possibility of using standard-shaped geometries to approximate complex structures, and the solution of such model converges to or approximates the continuous case with small enough elements, provided that the equilibrium of forces at the nodes and the compatibility of the displacements between elements are met (RAO, 2007, p. 725).

The first step of the procedure is the discretization the structural system into a number of finite elements (whose geometry is defined aiming the best approximation for the system) assumed to be interconnected by independently-displacing nodes on their boundaries, where each individual element will have a mechanical behaviour in accordance to the mechanical properties of the material and geometry attributed to it.

Afterwards, certain interpolation models (usually polynomial) are assumed for the solution of node displacements. The form of the three-dimensional displace for the e-th element, is, then:

$$\mathbf{u}^{(e)} = [N(x,y,z)]\mathbf{q}^{(e)}(t) \tag{2.43}$$

Where $\mathbf{u}$ and $\mathbf{q}$ are the displacement and nodal displacement vectors respectively, and $[N]$ is the matrix of the assumed shape functions. Using the matrix $[N]$ and the mechanical properties assumed for the element, it's possible to define stiffness, mass and damping matrices for each element, providing the following equations of motion for the e-th element (RAO, 2007, p. 731):

$$[M^{(e)}]\ddot{\mathbf{q}}^{(e)} + [C^{(e)}]\dot{\mathbf{q}}^{(e)} + [K^{(e)}]\mathbf{q}^{(e)} = \mathbf{f}^{(e)}(t) \tag{2.44}$$

With the element equations above, the system equations of motion can be obtained through a process of *element matrix assembly*. Each matrix (mass, stiffness and damping)

for the system will be the result of an operation on the element matrices as below (RAO, 2007, p. 731):

$$[M] = \sum_{e=1}^{E} [\alpha^{(e)}]^T [M^{(e)}][\alpha^{(e)}]$$
$$[K] = \sum_{e=1}^{E} [\alpha^{(e)}]^T [K^{(e)}][\alpha^{(e)}]$$
$$[C] = \sum_{e=1}^{E} [\alpha^{(e)}]^T [C^{(e)}][\alpha^{(e)}]$$

Here, the sums are over all of the E elements of the system, and $[\alpha^{(e)}]$ is the *connectivity matrix* of the e-th element of the system. The nodal displacement $\mathbf{q}^{(e)}$ and the vector of nodal unknowns $\mathbf{Q}$ are related by the connectivity matrix:

$$\mathbf{q}^{(e)} = [\alpha^{(e)}]\mathbf{Q} \tag{2.45}$$

So finally, the system equations in matrix form are given by:

$$[M]\ddot{\mathbf{Q}} + [C]\dot{\mathbf{Q}} + [K]\mathbf{Q} = \mathbf{F}(t) \tag{2.46}$$

Applying the boundary conditions imposed to specific elements, then, allows for the solution of the nodal displacements and, if needed, obtention of element strains and stresses.

2.3.3.1 Eigenvalue extraction

Once the application of the finite element procedure provides a matrix equation of the above form, finding its natural frequencies becomes an *eigenvalue extraction* problem. While there are several methods of real eigenvalue extraction, efficiency becomes an instrumental characteristic of the selected method once complex geometries are simulated (and, consequently, a high number of elements is used for approximating them) (INOYAMA, 2003).

Two classes of extraction methods are of main interest here: *Transformation methods*, which first manipulate the eigenvalue equation aiming for providing easier extraction; and *Tracking methods*, which extract eigeinvalues from the original equation iteratively, one at a time (INOYAMA, 2003).

In the pursuit of higher efficiency, hybrid methods have been developed which incorporate elements of both Transformation and Tracking methods (INOYAMA, 2003).

One example of this is the *Lanczos algorithm* (which will be indirectly used later in this work) (GOLUB; LOAN, 2013, p. 545) for solving the problem of the type:

$$-[M]^{-1}[K]\mathbf{v} = [A]\mathbf{v} = \lambda\mathbf{v} \tag{2.47}$$

Where $[A]$ is an Hermitian or real symmetric matrix (GOLUB; LOAN, 2013, p. 545) - which in the case of vibration problems translates into the need for the mass matrix to be positive semi-definite and the stiffness matrix to be symmetric (INOYAMA, 2003). The Lanczos method uses a series of steps to obtain a new matrix $[T]$ which is orthogonally related to the original $[A]$, but taking the simpler tridiagonal form (GOLUB; LOAN, 2013, p. 549):

$$[T] = \begin{pmatrix} \alpha_1 & \beta_2 & & & & 0 \\ \beta_2 & \alpha_2 & \beta_3 & & & \\ & \beta_3 & \alpha_3 & \ddots & & \\ & & \ddots & \ddots & \beta_{m-1} & \\ & & & \beta_{m-1} & \alpha_{m-1} & \beta_m \\ 0 & & & & \beta_m & \alpha_m \end{pmatrix} \tag{2.48}$$

And then finds its eigenvalues instead, as the eigenvalues of the set of matrices $\{T_k\}$ are easier to obtain and are progressively better estimates of the extremal (smallest and largest) eigenvalues of $[A]$ (GOLUB; LOAN, 2013, p. 546), what makes the method very efficient in finding some of the first fundamental frequencies and modes (corresponding eigenvectors) of systems as above.

2.3.3.2 Normalization of eigenvectors

Once the desired set of eigenvalues are extracted and their corresponding eigenvectors are found, the latter can be normalized to reflect *unitary modal masses* or *unitary maximum modal displacements* behaviour, due to their orthogonality properties. Specifically using the PATRAN/Nastran package, the eigenvectors can be normalized by using the MASS and MAX normalization options during eigenvalue extraction. To achieve *mass normalization*, for example, for an obtained modal matrix $\mathbf{\Phi}$, it must incur that (MSC-PATRAN..., , 2020):

$$\mathbf{\Phi}^T[M]\mathbf{\Phi} = [M_m] = [I] \tag{2.49}$$

Which means, of course, that every modal mass (for each vibration mode and natural frequency) is unitary. Maximum modal displacement normalization will be used later in section 3 to achieve simpler means of node displacement ratio calculation, for example.

2.4 Experimental vibration

As proposed earlier in section 2.1.1, we should now concern ourselves with the problem of, given a certain observed response, determining what is the model that predicts such behaviour in a system. Because the approach of this work relies more on simulation techniques than on experimental procedures, the reader is encouraged to pursue the theoretical basis of *experimental modal analysis* in the literature (CRAIG Jr; KURDILA, 2006; RAO, 2007; RAO, 2017; SILVA, 2007), which will not be developed here. Other topics such as active and hybrid vibration control, actuators for vibration control experiments and transducer localization are of paramount importance to the matter as well, and should be thoroughly considered for future, more experimentally inclined works.

A little more attention will be given here, accordingly, to possible damping estimation techniques as the groundwork for future developments in this realm, which should more appropriately compare the expected damping performances with and without external vibration control systems.

2.4.1 Dealing with damping

As will be later seen, in active and hybrid vibration control applications, the influence of the considered damping parameters (ζ and its corresponding linear c) in the model is frequently orders of magnitude lower than the damping provided by the control system itself. This can justify the absence of such parameters ($\zeta = c = 0$) in initial time- and frequency-response simulations as to handle the "worst case scenario" for the mechanical response of the system modelled, which will be exemplified in section 3.

To achieve an even more precise model, however, several approaches can be taken to figure out, either hypothetically or experimentally, the mechanical damping matrix [C] and its influence on the response of the system, what is usually done at the system level rather than at a individual element level (CRAIG Jr; KURDILA, 2006).

An easy first approach would be to assume a constant (across all frequencies) damping parameters ζ intrinsic to the structure. Values of 2% ($\zeta = 0.02$) are usually utilized as a first approximation, however through some specific hypotheses we could consider the $[C]$ matrix to be, for example, *proportional* to the matrices [M] and [K], achieving the so called *Rayleigh damping* case (CRAIG Jr; KURDILA, 2006), where:

$$[C] = \alpha_c[M] + \beta_c[K]$$

So now, applying the damping matrix as assumed above in the modal equations of motion (Equation 2.26) allows for the assumptions to provide, given two distinct natural frequencies ω_i and ω_j and their respective damping factors ζ_i and ζ_j, a way to find α_c and β_c (CRAIG Jr; KURDILA, 2006):

$$\zeta_{i,j} = \frac{\alpha_c + \beta_c \omega_{i,j}^2}{2\omega_{i,j}}$$

Finding such damping factor values can be done through a more experimental approach, through the use of techniques such as the *logarithmic decrement method* (CRAIG Jr; KURDILA, 2006; RAO, 2017), by allowing the structure to vibrate freely in the desired frequencies and, approximating it by a SDOF system, measuring two sequential peaks in position (amplitudes X_1 and X_2), which should decay approximately exponentially. The damping ratio in this frequency, then, can be approximated as:

$$\zeta_i = \frac{1}{2\pi} ln(\frac{X_{i,1}}{X_{i,2}})$$

Other types of non-viscous damping (e.g. Coulomb, structural, drag, hysteretic, modal) will not be considered in the present approach and can be readily found in the literature (CRAIG Jr; KURDILA, 2006; RAO, 2007; RAO, 2017). In any case, any of them can be approximated as an *equivalent viscous damping* by measuring the dissipated energy in each cycle, $W_{i,D}$, for each frequency ω_i of interest (CRAIG Jr; KURDILA, 2006):

$$c_{i,eq} = -\frac{W_{i,D}}{\pi \omega_i X_i^2}$$

2.5 Piezoelectric theory

As defined in the literature, the piezoelectric effect is the electric polarization behaviour certain materials (piezoelectric materials) present when subject to mechanical strains (direct effect), and vice-versa (converse effect) (ERTURK; INMAN, 2011), where the internal stresses resulting from the electric field are proportional to the electric field itself (or the other way around) (LANDAU; LIFSHITZ, 2013c, p. 68).

The underlying, fundamental principle driving such behaviour relies on the occurrence of asymmetries on the lattice of the material in question (JOOS; FREEMAN, 2013, p. 792), provided its ionic charges, when under deformation, give rise to a dipole moment. That, of course, means that in a lattice which intrinsically doesn't respond with charge imbalances to mechanical deformations the effect can't take place.

However, for example, consider the following crystal structure in the shape of a regular tetrahedron as exemplified below (Figure 6), where negative charges surround and balance a central positive charge:

When the once electrically balanced structure undergoes a certain deformation, if the resulting geometrical centre of the negative charges diverge from the position of the positive charge, an axis is created whose normal plane is not a plane of symmetry for the

Figure 6 – Tetrahedron lattice structure before (left) and after (right) mechanical strain

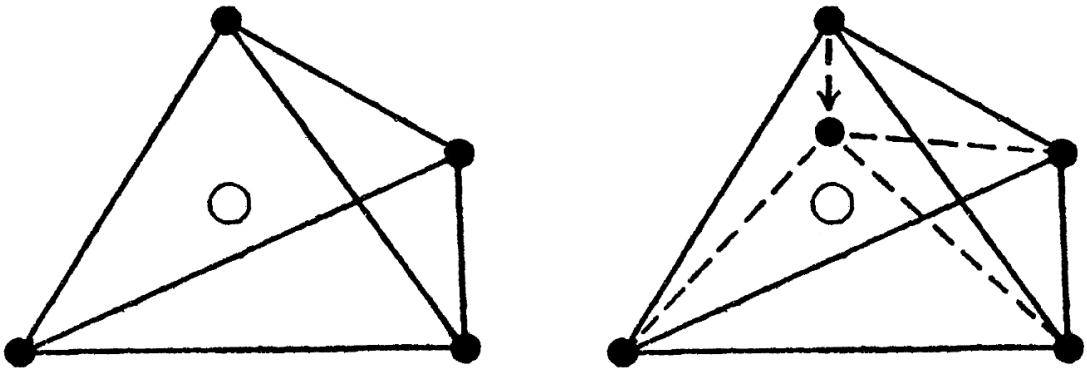

Source: (JOOS; FREEMAN, 2013, p. 792)

structure - what is called a polar axis. As a result, a dipole moment is created and the (direct) piezoelectric effect takes place (JOOS; FREEMAN, 2013, p. 792).

The application of the described phenomena to the coupling between the mechanical and the electrical realms of certain systems has been thoroughly studied since its discovery in 1880, especially from the 1950s onwards (ERTURK; INMAN, 2011), and has received extensive attention in the recent past due to its ample possibilities of usage in energy harvesting (SAFAEI; SODANO; ANTON, 2019), (ERTURK; INMAN, 2011), vibration mitigation and NVH control (GRIPP; RADE, 2018), robotics, Micro-Macro-Manipulators, MEMS, among many others.

Although piezo-polymers have been recently experiencing a fast growth due to several reasons (SAFAEI; SODANO; ANTON, 2019), the usual form of the mentioned piezoelectric materials is either a natural crystal (e.g. quartz, Rochelle salt) or an engineered piezoelectric ceramic. The latter provides an enhanced electrical-mechanical coupling, being the usual choice for engineering applications (ERTURK; INMAN, 2011), with its most popular representative being the Lead Zirconate Titanate (PZT) material developed in the 1950s (AMERICANPIEZO'S. . . , , 2020).

We shall hereinafter reasonably assume linear piezoelectric behaviour on the materials used and, as such, treat them as linear piezoelectric continua. Starting from the first law of thermodynamics applied to the latter, one can manipulate their way to the so called *Piezoelectric Constitutive Equation*, which relates mechanical stress and strain tensors, and electrical displacement and field tensors. Straightforward as such development might be, the thorough treatment extensively provided by the literature (ERTURK; INMAN, 2011; JALILI, 2009) renders unnecessary its exposure here, so a simple presentation of the constitutive equations themselves satisfies the purpose of this theoretical introduction:

$$T_{ij} = c^E_{ijkl} \cdot S_{kl} - e_{kij} \cdot E_k$$
$$D_i = e_{ikl} \cdot S_{kl} + \varepsilon^S_{ik} \cdot E_k$$

The above set of equations provides a linear unbounded piezoelectric model, where any form of A^B means A is evaluated assuming B constant, and c_{ijkl}, e_{kij} and ε_{ik} are respectively the elastic, piezoeletric and permittivity constants of the material. D and E are electric-domain variables (electric displacement and field, respectively), and S and T are mechanical-domain variables (strain and stress, respectively) (ERTURK; INMAN, 2011).

Assuming some limiting hypotheses, the bounded linear model can be represented by the following set of tensor equations (ERTURK; INMAN, 2011; INSTITUTE OF ELECTRICAL AND ELECTRONICS ENGINEERS, 1987):

$$S_{ij} = s^E_{ijkl} \cdot T_{kl} + d_{kij} \cdot E_k$$
$$D_i = d_{ikl} \cdot T_{kl} + \varepsilon^T_{ik} \cdot E_k$$

Which is analogous to the matrix representation used by the literature on the applications of piezoelectricity to vibration control (JALILI, 2009) (ERTURK; INMAN, 2011, p. 343), as later developed:

$$\begin{bmatrix} D \\ S \end{bmatrix} = \begin{bmatrix} \varepsilon^T & d \\ d^T & s^E \end{bmatrix} \cdot \begin{bmatrix} E \\ T \end{bmatrix} \tag{2.50}$$

Here d is an alternative form of the matrix of piezoelectric constants and s is the compliance matrix relating mechanical stress and mechanical strain (ZHOU; THOUVEREZ; LENOIR, 2014b).

The presented stub-like introduction to piezoelectric systems shouldn't be taken as a formal exposure of the subject, but rather as a motivation, using some relevant results, for the sequence of modelling techniques and assumptions taken in later sections.

2.5.1 3-1 operation mode

When the tensor constitutive relations of the piezoelectric material are studied, the conclusion can be drawn voltage, electric field, mechanical stress and mechanical strain can each be applied in at least three directions. Our bending application, however, will be concerned with a specific electromechanical relationship taking place between the axial (poling direction 1) and longitudinal (poling direction 3) axes, where mechanical influences in the former give rise to electrical consequences in the latter, and vice-versa. Figure 7

below illustrates this behavior for a piezoelectric patch of dimensions l, w and t for its length, width and thickness, respectively (LU; LEE; LIM, 2003).

Figure 7 – 3-1 operation mode

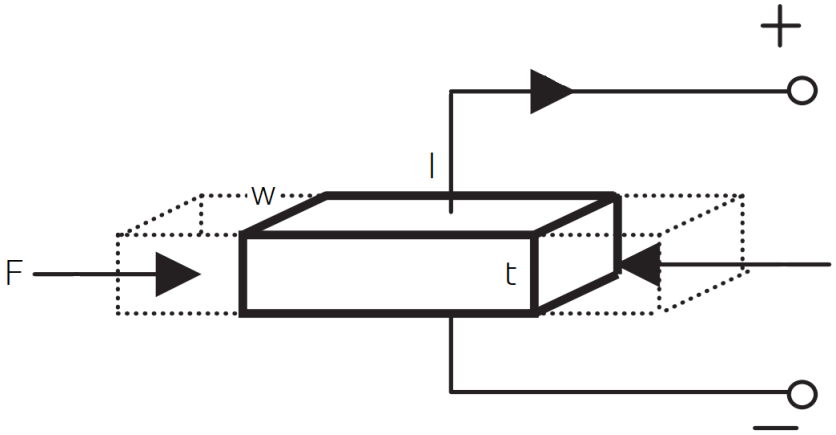

Source: (LU; LEE; LIM, 2003)

In this configuration, the piezoelectric constant d_{31}, the permittivity constant ε_{33}, and the mechanical compliance constant s_{11} are of primary relevance, while the mechanical variables S and T can be reduced to the 1-direction only and the electrical variables D and E can be reduced to the 3-direction only.

2.5.2 Single degree of freedom model

Let us now consider the single degree of freedom (SDOF) approximation for a piezoelectric patch as a thin beam of length l, width w and thickness t (ERTURK; INMAN, 2011, p. 344), and work our way back to a system of equations which can be readily implemented under such hypotheses. The first thing to be noticed is that a piezoelectric transducer patched onto the surface of a transversally vibrating body will operate in the d_{31} mode (JALILI, 2009, p. 198). In this case, from the tensor equations 2.50, we can eliminate specific stresses:

$$T_{2,3,4,5,6} = 0$$

With which equation 2.50 becomes (GRIPP; RADE, 2018):

$$\begin{bmatrix} S_1 \\ D_3 \end{bmatrix} = \begin{bmatrix} s_{11}^E & d_{31} \\ d_{31} & \varepsilon_{33}^T \end{bmatrix} \cdot \begin{bmatrix} T_1 \\ E_3 \end{bmatrix} \tag{2.51}$$

In this case, the electrical displacement D_3 and the axial mechanical strain S_1 take the following forms:

$$D_3 = \frac{Q}{wl} \tag{2.52}$$

Where Q is the accumulated electrical charge on a piezoelectric patch of surface area $A = wl$; and, for small enough displacements:

$$S_1 = \frac{x}{l} \tag{2.53}$$

The electrical field E_3 across the transducer relates linearly to the Voltage V:

$$E_3 = \frac{V}{t} \tag{2.54}$$

And the mechanical stress T_1, along the length of the patch, assuming a forcing condition on its end, is simply:

$$T_1 = \frac{F_p}{wt} \tag{2.55}$$

Then, knowing that for the SDOF case we have the tensors as scalars in the piezoelectric constitutive equation, then $d_{31}^T = d_{31}$, and equation 2.51 can be simply written as:

$$D_3 = \varepsilon_{33}^T E_3 + d_{31} T_1 \quad \Rightarrow \quad \frac{Q}{wl} = \varepsilon_{33}^T \frac{V}{t} + d_{31} \frac{F_p}{wt} \tag{2.56}$$

$$S_1 = d_{31} E_3 + s_{11}^E T_1 \quad \Rightarrow \quad \frac{x}{l} = d_{31} \frac{V}{t} + s_{11}^E \frac{F_p}{wt} \tag{2.57}$$

Or, rearranging for Q and F_p (GRIPP; RADE, 2018):

$$\begin{aligned} Q &= C_p V + \alpha_p x \\ F_p &= -\alpha_p V + K_p x \end{aligned} \tag{2.58}$$

With constants:

$$\alpha_p = \frac{w d_{31}}{s_{11}^E} \qquad K_p = \frac{wt}{l s_{11}^E} \qquad C_p = \frac{wl}{t}(\varepsilon_{33}^T - \frac{d_{31}^2}{s_{11}^E})$$

Here, the new constants have a more concrete meaning, where C_p is the piezoelectric output capacitance, K_p is the piezoelectric patch inherent stiffness, and α_p is the electromechanical coupling factor (GRIPP; RADE, 2018), (TOIT, 2005, p. 64).

Here and throughout this work it's going to be assumed that the piezoelectric element behaves linearly over all frequencies, which is not necessarily the case for usual piezoelectric materials yet is a precise enough approximation to justify its use here (TOIT, 2005, p. 68).

The piezoelectric relations in this form permit its use in a straightforward manner in a SDOF mechanical approximation – where F_p can be implemented in Newton's second law – once the voltage-charge behaviour $V(Q)$ has been studied, what fundamentally depends on the electrical circuit (whether real or notional) accompanying the piezoelectric transducer. This, of course, is precisely what will be done in a first approximation of the vibration control problem formerly proposed. It should be made evident here that the force F_p is along the length (direction 1) of the piezoelectric patch, as well as its resulting elongation represented by x. The transformation between the length-wise force and elongation F_p and x and their effective single-degree-of-freedom system counterparts will be discussed later, as their dynamic response results can be analysed in the piezoelectric patch's frame of reference without loss of generality.

2.5.3 Higher order models

For higher order models of piezoelectric patches and their applications to the control of vibrating structures, several references can be consulted from the literature (ERTURK; INMAN, 2011; GRIPP; RADE, 2018; JALILI, 2009). Such approaches will not be included here, however, as this stance does not necessarily translate into better simulation procedures for the moment, given the level of approximation so far used for the piezoelectric behaviour.

2.5.4 Piezoelectric applications to vibration control

In the pursuit of achieving vibration attenuation efficiency while under weight, energy consumption and costs constraints, the past decades have driven research towards the usage of the so called Smart Materials, which provided several innovative possibilities for such class of engineering challenges (GRIPP; RADE, 2018), delivering multi-domain physical coupling in distinct forms, of which we will develop discussions specifically on the electromechanical realm provided by piezoelectric circuits.

As with any vibration control application, piezoelectric transducers might be applied in both active and passive control techniques. Due to the inherent possible drawbacks of active control strategies – e.g. stability issues, power amplification needs (GRIPP; RADE, 2018) – this section will concentrate only in passive techniques, more specifically to shunt circuits.

This technical practice consists of using a piezoelectric transducer as a bridge between a vibrating system and an electric circuit intended for energy dissipation (shunt

circuit), by the means of the previously described direct piezoelectric effect (ERTURK; INMAN, 2011; GRIPP; RADE, 2018). The greater the transition of mechanical strain energy into dissipated electrical energy, the better the performance of the technique (ZHOU; THOUVEREZ; LENOIR, 2014a). In Figure 8, a simple representation of such assembly can be seen (GRIPP; RADE, 2018).

Figure 8 – SDOF system with piezoelectric and shunt circuit attachment

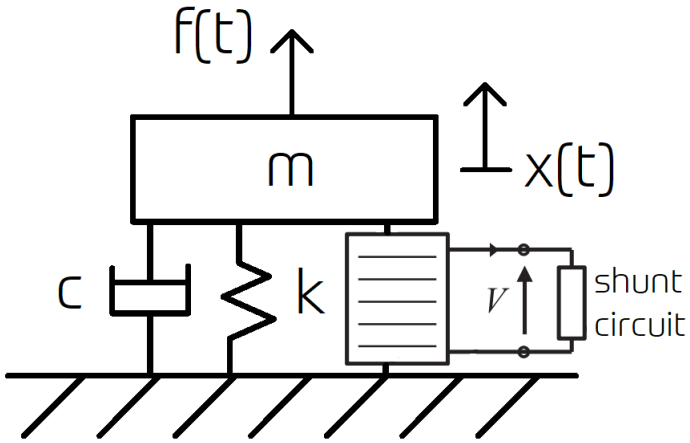

It should be noted that the damping performance of shunted piezoelectric patches highly depends on two distinct processes: the absorption of vibration (strain) energy into the patch (which depends on the modal behaviour of the structure and the strain energy distribution throughout its geometry, and consequently on proper patch location); and the capability of the piezoelectric materials to convert strain energy into electrical energy in its internal electric fields (which is determined by the piezoelectric electromechanical coupling effect) (ZHOU; THOUVEREZ; LENOIR, 2014a).

Because of such relationships, it is of the highest importance to achieve proper transducer localization, and the connection between different vibration modes (e.g. geometric strain energy distribution) and piezoelectric output voltage perfectly illustrates the need for proper location, and while it does not lie in the scope of this introduction, a brief review of piezoelectric positioning is provided in the literature (GRIPP; RADE, 2018).

Undemanding as they might be, linear piezoelectric shunt circuits present an inherent hurdle: specific resonance frequency tuning due to their linear behaviour might expressively reduce attenuation performance in different frequencies of vibration (JALILI, 2009; SILVA et al., 2018; ZHOU; THOUVEREZ; LENOIR, 2014a). For any (piezoelectric or otherwise) passive damping system, energy dissipation and overall performance is best only within its highest sensitivity frequency region (JALILI, 2009). While improvements can be made by system parameters optimization or the use of semiactive systems (JALILI, 2009), a greater resonance frequency range that can be inherently achieved with nonlinear

circuits (ZHOU; THOUVEREZ; LENOIR, 2014a), for example.

While several types of electric and electronic shunt circuits have been studied, applied and reviewed in recent works (CORR; CLARK, 2002; GRIPP; RADE, 2018), including Adaptive shunt circuits and Switching shunt circuits (which can, indeed, achieve significant adaptation to different excitation frequencies), the focus of our discussions hereafter will be on an intrinsically nonlinear class of circuits known as Nonlinear Energy Sinks.

2.5.5 Nonlinear energy sinks

The mathematical basis of the interaction between linear vibrating systems and a nonlinear system with the purpose of obtaining energy transfer from the former to the latter has been formulated since the 2000's in the works of several scientists and engineers (GENDELMAN, 2001; GENDELMAN et al., 2001; GENDELMAN; STAROSVETSKY; FELDMAN, 2008; STAROSVETSKY; GENDELMAN, 2008; STAROSVETSKY; GENDELMAN, 2009; VAKAKIS; GENDELMAN, 2001). Formerly proposed as a notional cubic-behaviour (GENDELMAN et al., 2001) or an n^{th} order polynomial-behaviour (GENDELMAN, 2001) oscillatory attachment, energy transfer to nonlinear systems has been thoroughly studied as a way to achieve one-way channelling of vibration energy with no preferential resonance frequency (GENDELMAN et al., 2001), giving rise to the concept of a *Nonlinear Energy Sink* (NES).

While several straightforward and artful mechanical and electromechanical nonlinear energy sinks have been investigated and applied in the literature, special attention will be given to the piezoelectric NES concept described in some recent works (SILVA et al., 2018; VIGUIÉ; KERSCHEN; RUZZENE, 2009; ZHOU; THOUVEREZ; LENOIR, 2014a; ZHOU; THOUVEREZ; LENOIR, 2014b) because of its alignment with the problem investigated in this work.

The present section will not develop the elegant mathematical theory modelling the interaction between linear and nonlinear systems, but will focus instead on the brief description of the physical features of a piezoelectric nonlinear energy sink. Let's consider, then, the piezoelectric element to be attached to a shunt circuit taking the notional form below (Figure 9):

Here, the R, L and C elements are of course the resulting resistance, inductance and capacitance elements of the circuit, while the fourth NL element is a general non-linear element which might brake the linearity of voltage-charge (or voltage-current) relationship in any form. Several references in the literature have proposed different approaches as to how to model and obtain this non-linear factor (SILVA et al., 2018; TRIPLETT; QUINN, 2009; ZHANG; TANG; LIU, 2017; ZHOU; THOUVEREZ; LENOIR, 2014a) Let's then

Figure 9 – Representation of a shunt circuit with a nonlinear element.

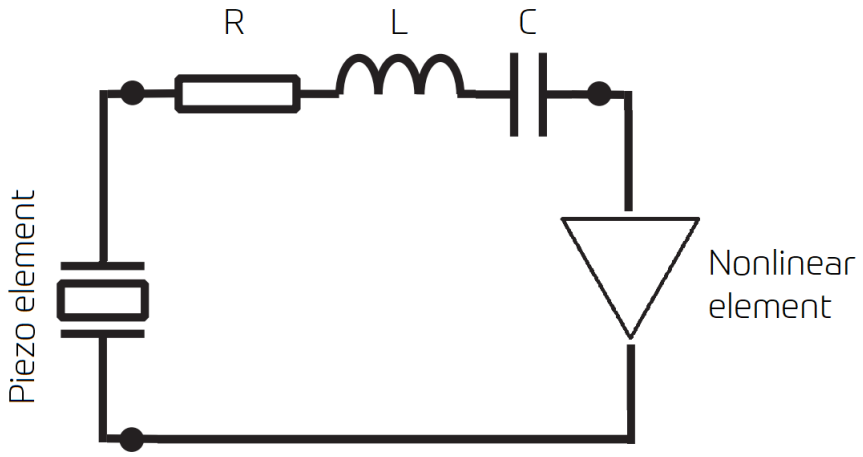

consider a cubic behaviour for such form:

$$V_{nl} = \alpha_{nl} q^3 \tag{2.59}$$

We can make use of *Kirchhoff's voltage law* to deduce the differential equation of the circuit:

$$V_p = V_R + V_L + V_C + V_{nl} \tag{2.60}$$

By inserting then each element's voltage drop into this equation, we have as a result another expression for the piezoelectric voltage V_p:

$$V_p = R\dot{q} + L\ddot{q} + \frac{1}{C}q + \alpha_{nl} q^3 \tag{2.61}$$

Now, from the previous section, we know that the piezoelectric voltage inherently takes a linear form between the element's elongation and charge as provided by equation 2.58. Rearranging its terms to find the voltage (TRIPLETT; QUINN, 2009):

$$V_p = -\frac{\alpha_p}{C_p} x + \frac{1}{C_p} q \tag{2.62}$$

The above two equations when put together result in the electrical domain differential equation for this notional system:

$$L\ddot{q} + R\dot{q} + (\frac{1}{C} - \frac{1}{C_p})q + \alpha_{nl} q^3 + \frac{\alpha_p}{C_p} x = 0 \tag{2.63}$$

As we are dealing with a notional circuit anyways, we might as well generalize the physical constants of this equation for future ease of manipulation:

$$\alpha_0\ddot{q} + \alpha_1\dot{q} + \alpha_2 q + \alpha_{nl}q^3 + \alpha_4 x = 0 \tag{2.64}$$

The equation above provides the behaviour that will be considered for the electrical domain of our nonlinear energy sink throughout this work. As explained in the literature (SILVA et al., 2018), the linear term $\alpha_2 = 1/C - 1/C_p$ here has a great influence on the broadband attenuation performance of the NES system, and should be ideally zero. In other words, the equivalent capacitance C should be designed in such a way that α_2 is as close to 0 as possible without being compromising to the physical feasibility of the circuit.

2.5.6 Piezoelectric transducer localization

Taking into account the previously noted relationship between vibration attenuation effectiveness and geometric strain distribution (ZHOU; THOUVEREZ; LENOIR, 2014b), the location of the piezoelectric transducer is of paramount importance to the design of the vibration control system (GRIPP; RADE, 2018). For a continuous system, having certain target vibration modes in mind allows for the appropriate positioning of the transducer to maximize the piezoelectric voltage output and, as such, the energy transfer from the structure to the electrical domain (KANG et al., 1996).

So, without delving too much into the intricacies of optimal transducer localization, we can reasonably assume that the higher the final strain under which the piezoelectric element is subjected, given its constitutive equations, the higher is its capacity to pump vibration energy into the electrical domain. For a cantilever blade, then, considering for example its first mode of vibration, we should position the piezoelectric patch as close to the clamped end as possible as so to maximize transverse position differences between the ends of the piezoelectric element.

3 MODELLING AND SIMULATION DEVELOPMENT

Now with the basics of the theory of vibrations and piezoelectric systems laid out, we can proceed to their implementation in solving the motivating problem explored in the first chapter. To do so, the approach here used will be of first modelling the freely vibrating and controlled blade cases, then obtaining solutions (approximate analytical, numerical and experimental) to the blade vibration parameters, and finally followed by the proposal of application of experimental setups for the blade and bladed disk vibration problems, pointing out possible implementations according to the studies here developed and to the literature. It will be clear for the reader that the bulk of the development of this work will be dealing with the modelling and simulation of the current control problem, while experimental applications themselves will be kept for future works.

As will be seen, we can easily approximate the behaviour of our system through a single-degree-of-freedom approximation for its mechanical domain, with its applicability being a matter of whether or not the considered (usually the fundamental) mode of vibration is dominant enough, and references to higher-order models on the literature will be introduced when pertinent throughout the development of the theory and its applications.

3.1 Blade and blade-NES models

3.1.1 Single-degree-of-freedom model

The first step towards finding a single-degree-of-freedom model approximating the system's behaviour should be obtaining its vibration modes and, from them, deriving for each a generalized mass and stiffness which can then be modelled into a mechanical-domain differential equation.

Our approach to the obtention of a model for the NES-controlled vibrating blade will make use of the SDOF mechanical (GRIPP; RADE, 2018; SILVA et al., 2018; ZHOU; THOUVEREZ; LENOIR, 2014a) and SDOF piezoelectric (GRIPP; RADE, 2018; ZHOU; THOUVEREZ; LENOIR, 2014a) models discussed previously in chapter 2. We obtain, as seen, the mechanical response in the form:

$$m\ddot{x} + c\dot{x} + (k + k_p + \frac{a_p^2}{Cp})x - \frac{\alpha_p}{C_p}q = f(t) \tag{3.1}$$

In the specific case of a base excitation motion where the only forces acting on the

mass m come from the stiffness, damping and piezoelectric elements, we have:

$$m\ddot{x}_2 + c(\dot{x}_2 - \dot{x}_1) + (k + k_p + \frac{\alpha_p^2}{C_p})(x_2 - x_1) - \frac{\alpha_p}{C_p}q = 0 \tag{3.2}$$

And assuming a cubic voltage-charge behaviour for the electrical domain, we can propose the following behaviour for the electrical domain, for any instant charge $q(t)$ (SILVA et al., 2018) (where $x = x_2 - x_1$ for the base excitation case, of course):

$$\alpha_0\ddot{q} + \alpha_1\dot{q} + \alpha_2 q + \alpha_{nl}q^3 - \frac{\alpha_p}{C_p}x = 0 \tag{3.3}$$

Where the constants α_0, α_1, α_2 and α_{nl} would be functions of the physical elements' constants (resistance, capacitance and impedance) in a real analogical circuit, while α_p depends on the piezoelectric and mechanical constants of the transducer (GRIPP; RADE, 2018; ZHOU; THOUVEREZ; LENOIR, 2014a).

As will be seen, the model provided by equations 3.1 (or sometimes 3.2) and 3.3 does provide a great insight on the nonlinear behaviour of this piezo-electro-mechanical system. However, it should be noted that, because we are dealing with the modal coordinate of our mechanical system, this model still does not represent perfectly the interaction between the piezoelectric element (whose behaviour is modelled in axial elongation coordinates) and the blade (which is brought to a single-degree-of-freedom modal system for each of its natural frequencies). To achieve a better representation, once the modal analysis of the blade is performed we will deal with the relationship (which will be assumed linear) between those two different coordinates and update accordingly the models and transfer functions here and now obtained.

3.1.2 SDOF transfer functions, general forcing

We might also like to generalize the response behaviour between position, or speed, and the force input. To assess that, let's obtain the transfer function for a system which takes a generalized form of equations 3.1 and 3.3:

$$\begin{aligned} \beta_0\ddot{x}(t) + \beta_1\dot{x}(t) + \beta_2 x(t) + \beta_3 q(t) &= f(t) \\ \alpha_0\ddot{q}(t) + \alpha_1\dot{q}(t) + \alpha_2 q(t) + \alpha_3 q^3(t) + \alpha_4 x(t) &= 0 \end{aligned} \tag{3.4}$$

By taking the Laplace transform (ÅSTRÖM; MURRAY, 2010) of the equations above:

$$[\beta_0 s^2 + \beta_1 s + \beta_2]X(s) + \beta_3 Q(s) = F(s) \tag{3.5}$$

$$[\alpha_0 s^2 + \alpha_1 s + \alpha_2]Q(s) + \alpha_3 \mathcal{L}(q^3) + \alpha_4 X(s) = 0 \tag{3.6}$$

For finding $\mathcal{L}(q^3)$, let us recall the definition of the Laplace transform (ÅSTRÖM; MURRAY, 2010):

$$\mathcal{L}(f(t)) = \int_0^\infty f(t)\, e^{-st} dt \;\Rightarrow\; \mathcal{L}(q^3) = \int_0^\infty q^3\, e^{-st} dt \tag{3.7}$$

By integrating by parts twice, we arrive at:

$$\int_0^\infty q^3\, e^{-st} dt = \left[-\frac{1}{s}\, q^3\right]_0^\infty + \frac{3}{s}\left\{\left[-\frac{1}{s}\, q^2\right]_0^\infty + \frac{2}{s}\int_0^\infty q\, e^{-st} dt\right\} \tag{3.8}$$

So, reapplying the definition of the Laplace transform and taking the limits of integration for the terms on the right-hand side:

$$\int_0^\infty q^3\, e^{-st} dt = \frac{q(0)^3}{s} + \frac{3}{s}\left[\frac{q(0)^2}{s} + \frac{2}{s}Q(s)\right] \tag{3.9}$$

Finally, with the initial condition $q(0) = q(\infty) = 0$, we arrive at:

$$\mathcal{L}(q^3) = \frac{6}{s^2}\, Q(s) \tag{3.10}$$

Now, back at the transfer function in equation 3.6:

$$[\alpha_0 s^2 + \alpha_1 s + \alpha_2 + \frac{6\alpha_3}{s^2}]Q(s) + \alpha_4 X(s) = 0 \tag{3.11}$$

Which, together with equation 3.5, gives us the transfer function:

$$X(s) = \left\{\frac{1}{\beta_0 s^2 + \beta_1 s + \beta_2 - \frac{\beta_3 \alpha_4 s^2}{\alpha_0 s^4 + \alpha_1 s^3 + \alpha_2 s^2 + 6\alpha_3}}\right\} F(s) \tag{3.12}$$

Or:

$$\frac{X}{F}(s) = \frac{\alpha_0 s^4 + \alpha_1 s^3 + \alpha_2 s^2 + 6\alpha_3}{D_6 s^6 + D_5 s^5 + D_4 s^4 + D_3 s^3 + D_2 s^2 + D_1 s + D_0} \tag{3.13}$$

And, of course, for the speed $\dot{x}$:

$$V(s) = \left\{\frac{1}{\beta_0 s^2 + \beta_1 s + \beta_2 - \frac{\beta_3 \alpha_4 s^2}{\alpha_0 s^4 + \alpha_1 s^3 + \alpha_2 s^2 + 6\alpha_3}}\right\} F(s) \tag{3.14}$$

Or:

$$\frac{V}{F}(s) = \frac{\alpha_0 s^5 + \alpha_1 s^4 + \alpha_2 s^3 + 6\alpha_3 s}{D_6 s^6 + D_5 s^5 + D_4 s^4 + D_3 s^3 + D_2 s^2 + D_1 s + D_0} \tag{3.15}$$

Where, in both cases:

$$D_6 = \alpha_0\beta_0 \qquad D_2 = \alpha_2\beta_2 + 6\alpha_3\beta_0 - \alpha_4\beta_3$$
$$D_5 = \alpha_0\beta_1 + \alpha_1\beta_0 \qquad D_1 = 6\alpha_3\beta_1$$
$$D_4 = \alpha_0\beta_2 + \alpha_1\beta_1 + \alpha_2\beta_0 \qquad D_0 = 6\alpha_3\beta_2$$
$$D_3 = \alpha_1\beta_2 + \alpha_2\beta_1$$

3.1.3 SDOF transfer functions, base excitation and inertial excitation

Now if we consider once again the specific case where (Equation 3.2):

$$f(t) = c(\dot{x}_1 - \dot{x}_2) + k(x_1 - x_2) \tag{3.16}$$

We have, in the s-domain, the following relationship:

$$F(s) = (cs + k)(X_1 - X_2) \tag{3.17}$$

Which, when inserted into equation 3.5 (without the redundant stiffness and damping factors c and k acting on the mass m), provides:

$$[ms^2 + (k_p + \frac{a_p^2}{Cp})]X_2(s) - \frac{\alpha_p}{C_p}Q(s) = (cs + k)(X_1 - X_2) \tag{3.18}$$

By following the same procedure from the last section using the s-domain form of the system's electrical behaviour, we have:

$$[\alpha_0 s^2 + \alpha_1 s + \alpha_2 + \frac{6\alpha_3}{s^2}]Q(s) + \alpha_4(X_2(s) - X_1(s)) = 0 \tag{3.19}$$

Together, the two equations above provide the transfer function for the base motion case:

$$\frac{X_2}{X_1} = \frac{V_2}{V_1} = \frac{N_5 s^5 + N_4 s^4 + N_3 s^3 + N_2 s^2 + N_1 s + N_0}{D_6 s^6 + D_5 s^5 + D_4 s^4 + D_3 s^3 + D_2 s^2 + D_1 s + D_0} \tag{3.20}$$

Where its constants are:

$$
\begin{aligned}
D_6 &= \alpha_0\beta_0 & & \\
D_5 &= \alpha_0\beta_1 + \alpha_1\beta_0 & N_5 &= \alpha_0\beta_1 \\
D_4 &= \alpha_0\beta_2 + \alpha_1\beta_1 + \alpha_2\beta_0 & N_4 &= \alpha_0\beta_2 + \alpha_1\beta_1 \\
D_3 &= \alpha_1\beta_2 + \alpha_2\beta_1 & N_3 &= \alpha_1\beta_2 + \alpha_2\beta_1 \\
D_2 &= 6\alpha_2\beta_2 + 6\alpha_3\beta_0 - \alpha_4\beta_3 & N_2 &= \alpha_2\beta_2 \\
D_1 &= 6\alpha_3\beta_1 & N_1 &= 6\alpha_3\beta_1 \\
D_0 &= 6\alpha_3\beta_2 & N_0 &= 6\alpha_3\beta_2
\end{aligned}
$$

Notice that from the modelling provided in the previous section, we can easily assume an inertial forcing condition for the base excitation problem, in which $f(t)$ takes the form (SILVA et al., 2018):

$$f(t) = -ma_b(t) \tag{3.21}$$

Here, $a_b(t)$ is the base acceleration $\ddot{x_1}(t)$, which can take any form, but in the specific case where the base excitation is harmonic, of course so is its second derivative. Using this approach interchangeably with the stiffness and damping forcing condition (equation 3.16) should of course yield the same results by a simple change of variables $x = x_2 - x_1$.

3.2 Mechanical parameters

With the models of the problem presented as above, for predicting its behaviour or implementing our control approach we must first obtain the mechanical (m, c, k), piezoelectric (α_p, C_p, k_p) and electrical ($\alpha_{0,1,2,nl}$) parameters of the differential equations obtained. While the mechanical and piezoelectric parameters are intrinsic to the mechanical, geometrical and piezoelectric properties of our system, we can model our electrical-domain behaviour to achieve the greatest possible damping performance in our vibration control problem (SILVA et al., 2018), which later will be a circuit design issue but right now is intrinsically a matter of maximizing frequency- and time-response performance in our soon to be developed simulations. To get there, let's first concern ourselves with the modal analysis of our blade model.

3.2.1 Blade modal analysis: plate approximation quasi-analytical solutions

As a first approximation for the vibration modes of the blade, let's suppose it follows the behaviour of a vibrating plate of geometry (length, width and thickness) similar to the blade in question. In our case, the dimensions of the blade could be easily obtained

by its CAD model (Figure 10), and when the geometry of the blade diverged too much from that of a simple plate (which was the case for its width and thickness), the averages of measurements in several different points were taken as the final dimension, as exemplified by Figure 11.

Figure 10 – Blade CAD model render and views

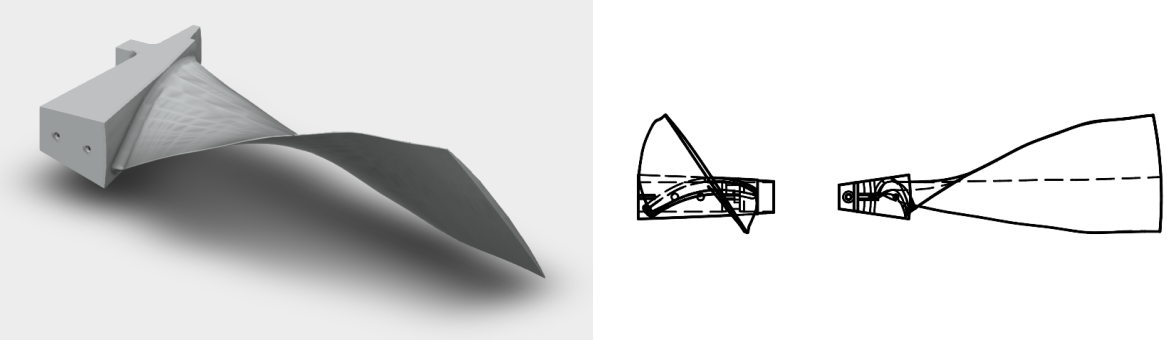

Figure 11 – Example of sample measurements on the blade model

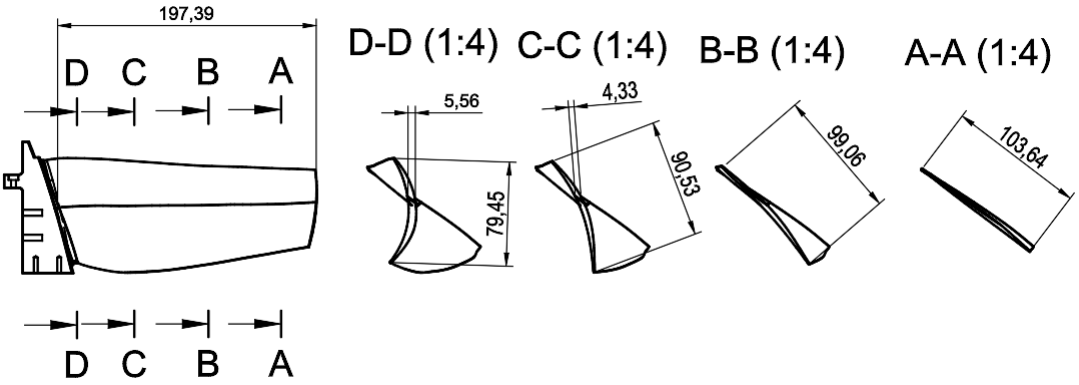

The resulting approximate values for the plate dimension are presented in Table 1, alongside its relevant physical properties (for Aluminium T7075).

Table 1 – Plate geometry and mechanical properties

Length (L, mm)	Width (w, mm)	Thickness (t, mm)
197	93	5
Poisson's ratio	Mass density (kg/m^3)	Elasticity module (Pa)
0.33	2810	7.17E+10

Then, as seen in section 2, its natural frequencies will be the solution of the following equation, for the n^{th} eigenvalue:

$$\omega_n = \frac{\lambda_n^2}{a^2}\sqrt{\frac{Eh^2}{12\rho(1-\nu^2)}} \tag{3.22}$$

The values of λ_n cannot be obtained analytically for the equation above, so a numerical reference for specific ratios L/w was taken from the literature (INOYAMA, 2003) as presented in Table 2 for the first eight vibration modes.

Table 2 – Approximate plate eigenvalues ($\nu = 0.33$) (INOYAMA, 2003)

Ratio L/w	1	2	3	4	5	6	7	8
2.0	3.42	14.50	21.28	37.32	59.76	91.24	92.68	177.70
2.5	3.41	17.58	21.24	56.14	59.72	104.30	117.10	143.40

Of course, in the case considered the ratio $L/w = 197/93$ is approximately 2.12, so the eigenvalues were obtained by linear interpolation from the available data. By the use of Equation 3.22, then, the approximate natural frequencies were obtained according to Table 3.

Table 3 – Approximate natural frequencies ($\nu = 0.33$, $L/w = 2.12$)

	1	2	3	4	5	6	7	8
λ_n	3.42	15.24	21.27	41.77	59.75	94.33	98.46	123.78
ω_n (rad/s)	680	3031	4233	8313	11891	18773	19595	24634
ω_n (Hz)	108.2	482.4	673.7	1323.1	1892.6	2987.8	3118.6	3920.7

Source: (INOYAMA, 2003)

3.2.2 Blade modal analysis: PATRAN-Nastran numerical solutions

For a second approximation of the vibration modes of the blade, the geometrical model in IGES format was imported into the MSC. PATRAN/Nastran package. After appropriate cleaning of the imported geometry using the Geometry features of the software and its user manual as reference (MSC-PATRAN. . . , , 2020), the faces associated with the attaching base of the blade were removed, just as done in Figure 1. The idea here is to simulate the blade as cantilevered by its bolster, what better approximates the blade-only vibration behaviour in a bladed disk and allows for a more precise mesh in the body of the blade itself.

The resulting surfaces were transformed into a solid using the B-rep conversion, and the simulation, meshing and solution parameters used for obtaining the natural frequencies and modes of vibration can all be found in table 4. Here the element type selected was a tetrahedron (TET10) because of its conformability to complex shapes (BROWN, 1997; INOYAMA, 2003), as the one of the twisted blade.

The load case used to simulate the blade-disk attachment was a restriction on the position and rotation as boundary conditions to the face cutting through the blade's shank. As expected in a complex geometry, some errors were found during pre-processing mesh

Table 4 – FEM Simulation Parameters

Pre-processing	Global tolerance	0.5 mm
	Element type	TET10
	Material	Al 7075
	Mesh resolution	5.0 mm
	Elasticity modulus	71.7 GPa
	# Elements	7405
	Poisson's ratio	0.33
	# Nodes	14588
	Mass density	2810 kg/m^3
	Load type	Displacement
Solution	Solver	MSC NASTRAN 2008
	Solution type	Modal analysis (103)
	Normalization	Maximum displacement
	Extraction method	Lanczos

examination by the software, yet easily dealt with by altering the meshing structure on an element level.

After running the solver, the solution data provided by the .f06 file generated for the eigenvalues and modes of vibration are presented in table 5. Of those values, the ones of highest interest for this application are the first natural frequencies and their vibration modes, so just as before the first eight frequencies are shown below.

Table 5 – FEM Simulation Results (PATRAN)

Mode	1	2	3	4	5	6	7	8
ω_n (Hz)	123.8	381.8	954.9	1069.6	1860.3	2022.2	2395.1	2835.6

The initial mesh structure for the blade and the fundamental vibration mode provided by the solver run can be visualized by Figure 12 below.

Figure 12 – Blade mesh before and after the PATRAN/Nastran solver run

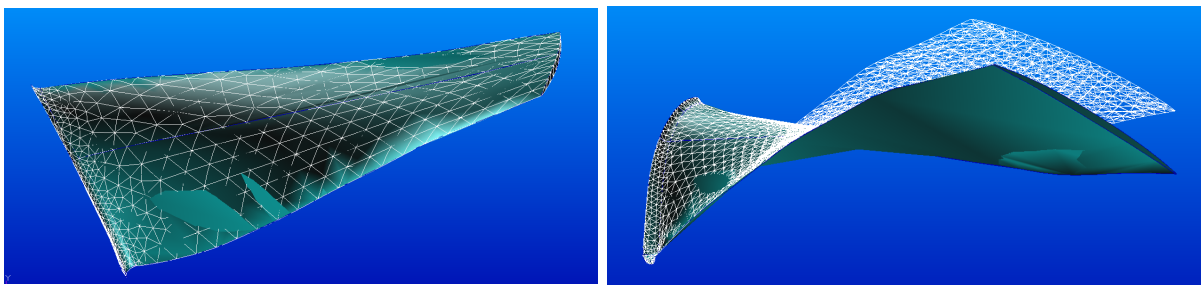

3.2.3 Blade modal analysis: Fusion 360 numerical solutions

Finally, we can also obtain yet another even more straightforward numerical prediction for the natural frequencies of the blade by the use of integrated CAD/CAE

packages such as the Autodesk Fusion 360 software. The procedure here is quite simple especially because of its integrated modelling and simulation environments, where in the former geometry cleaning and correction is readily available and in the latter important setup parameters (such as mesh geometry and specifications, solver type and extraction method) are automatically assigned to the pre-processing and solution.

The detailed results from this simulation can be explored in appendices and are summarized in table 6 below.

Table 6 – FEM Simulation Results (Fusion 360)

Mode	1	2	3	4	5	6	7	8
ω_n (Hz)	124.0	380.7	948.1	1054	1816	1960	2315	2725

3.2.4 Mass and stiffness parameters

With the solutions provided by the modal analysis explored above, we can attribute appropriate values to m and k in the mechanical model considered (equation 3.1). To each n-th specific vibration mode, we can associate a set of *generalized mass* and *stiffness* which provide its natural frequency ω_n (MSC-PATRAN. . . , ; RAO, 2007).

We can see that the agreement between the numerical solutions provided by both FEM packages (PATRAN and Fusion 360) is notably good, especially in the first five modes, as would be expected, in spite of the lack of leeway regarding mesh, solution and post-processing controls provided by integrated CAE packages such as the one used. The quasi-analytical rectangular plate model also provides a good approximation for the natural frequencies, but it's clear that the lower rigidity and inertia provided by the plate's uniform cross section (in comparison with the actual blade's twisted, U-like geometry) provides lower resonance frequencies as would be expected. The values obtained by the plate approximation, however, still provide a good sanity check as we can more confidently apply the FEM-obtained values in the assessment of our mechanical constants m and k.

If in the modal analysis process described in section 2 we normalize the modal matrix $\mathbf{\Phi}$ such that our modal mass matrix $[M_m]$ is unitary in each vibration mode, we obtain generalized masses $m = 1.0$ for every considered vibration mode and the generalized stiffness can be very straightforwardly obtained by squaring its corresponding natural frequency in radians. If, on the other hand, we normalize the maximum modal displacement solution, obtaining the relationship between the piezo element axial elongation and the modal coordinate is considerably easier, justifying its use for working around the problem laid out in the begining of this section. This is precisely what will be done for correcting our model, using the MSC Patran/Nastran simulation given its broader post-processing capabilities.

Now, for the generalized mass and stiffness parameters, such values are directly obtained from the simulation in the .f06 files provided in the appendices. Table 7 below shows such values (again, for normalized maximum modal displacements) on the first eight modes obtained.

Table 7 – Generalized mass and stiffness values

Mode	Frequency	$m_{gen}(kg)$	$k_{gen}(N/m)$
1	$1.24 \times 10^{+02}$	2.76×10^{-02}	$1.67 \times 10^{+04}$
2	$3.78 \times 10^{+02}$	1.96×10^{-02}	$1.12 \times 10^{+05}$
3	$9.47 \times 10^{+02}$	9.62×10^{-03}	$3.41 \times 10^{+05}$
4	$1.05 \times 10^{+03}$	1.47×10^{-02}	$6.43 \times 10^{+05}$
5	$1.82 \times 10^{+03}$	1.13×10^{-02}	$1.47 \times 10^{+06}$
6	$1.96 \times 10^{+03}$	9.99×10^{-03}	$1.52 \times 10^{+06}$
7	$2.33 \times 10^{+03}$	3.76×10^{-03}	$8.08 \times 10^{+05}$
8	$2.73 \times 10^{+03}$	1.06×10^{-02}	$3.12 \times 10^{+06}$

3.2.5 Correction of the single-degree-of-freedom model

To solve the inadequacy between the blade modal coordinate and the piezoelectric element axial coordinate, we are now able to update our model with the results from the FEM-based modal analysis.

To obtain realizable predictions for the damping performance of our piezoelectric system, some assumptions have to be made regarding the actual vibration of the blade (what we would be trying to minimize), and the supposed piezoelectric patch effect onto the blade itself. Probably the most compromising of such hypotheses will take place at this point of our conceptual model: a linear relationship between the axial elongation of the piezoelectric patch and the modal coordinate of the system will be assumed during any mode of vibration considered. For example, in the fundamental mode, to which the system is to be tuned, the elongation during peak blade deformation can be obtained from any FEM package as exemplified using MSC Patran/NASTRAN:

In this specific simulation instance, the nodes to be considered for such elongation are presented in Figure 13 below. These are nodes that start close to the blade root, where we intend to place our piezeoelectric patch, and span roughly the same distance as the length of the undeformed transducer (Midé Corp. QP10N) considered for this prediction. Of course the distance is not exactly the same, but nevertheless close enough to provide a reliable linear approximation. By directly measuring the distances between the relevant nodes before (rest) and after (peak deformation) the simulation, we can obtain the elongation caused in this area.

The MSC Patran/Nastran package also outputs a report, for specific vibration modes, showing the final deformation for specific nodes, which were selected according

Figure 13 – Nodes selected to represent the piezoelectric patch position

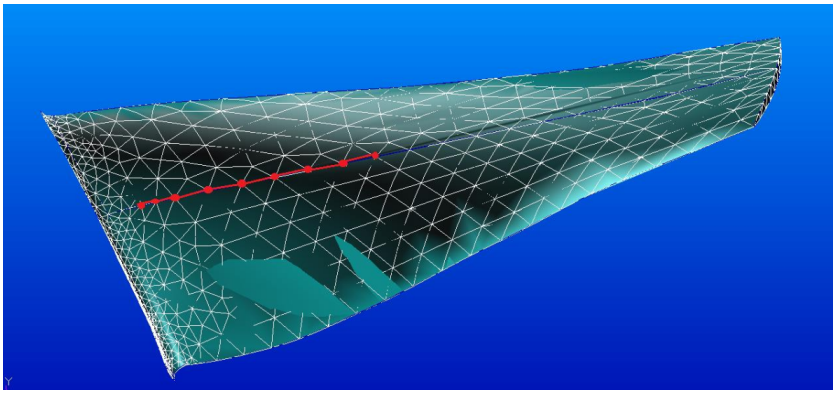

Figure 14 – Notional example of nodes before (top) and after (bottom) deformation

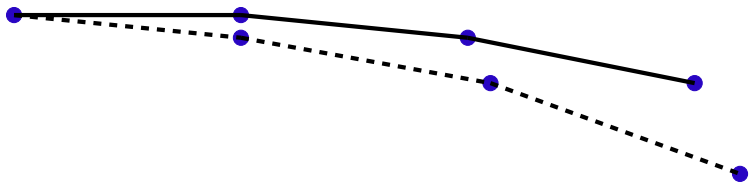

to Figure 13 and whose total deformations are presented below. With such individual deformations in hand, we can of course calculate the difference in position variation from one node to the next. Figure 14 exemplifies the geometry of the simple elongation problem we face here and its solution can be straightforwardly obtained from equation 3.23.

$$\Delta L_{nodes} = L^{i}_{nodes} - L^{f}_{nodes} \tag{3.23}$$

Where the original and final sums of distances are:

$$L^{i}_{nodes} = \sum_{i=1}^{N-1} \sqrt{\sum_{q=x,y,z} (q_i - q_{i-1})^2}$$

$$L^{f}_{nodes} = \sum_{i=1}^{N-1} \sqrt{\sum_{q=x,y,z} [(q_i + \delta^{q}_{i}) - (q_{i-1} + \delta^{q}_{i-1})]^2}$$

The values obtained from the process above for the fundamental mode, which is the one we are tuning or circuit to, are presented in table 8. By calculating the original distances between the nodes, and from their displacements in each coordinate calculating their final, post-deformation distances, we are able to obtain an approximation for the elongation of this chain of nodes, as provided by table . The detailed position and displacement results from the software can be seen in the appendices.

From the data sheet of our piezoelectric patch (Midé Corp. QP10N) (MIDé. . . , , 2020), we have the length of this transducer to be $L_{patch} = 45.974mm$. Approximating the

Table 8 – Distances and elongation of relevant nodes

Node	**Original distance**	**Final Distance**
9654	–	–
9656	5.0407	5.0399
9658	5.0410	5.0401
9660	5.0408	5.0399
9662	5.0405	5.0396
9664	5.0406	5.0397
9666	5.0409	5.0401
9668	5.0409	5.0402
9670	5.0408	5.0401
9672	5.0408	5.0402
Total	**45.3671**	**45.3598**
	Elongation	**0.0073**

total elongation to be linear in this region, we have the final axial deformation for our piezoelectric patch:

$$\Delta L_{patch} = \frac{L_{patch}}{L_{nodes}} \Delta L_{nodes} = \frac{45.974}{45.367} 0.0073 = 0.0074 \tag{3.24}$$

We thus need to obtain the maximum modal deformation for the first mode (which we are considering for our simulation) so the aforementioned linear relationship can be traced. In any non-normalized case this could be easily obtained from the uncoupled equations of motion of this mode, as seen in section 2, with the constants provided by the generalized mass and stiffness:

$$m_{gen}\ddot{x}(t) + k_{gen}x(t) = 0 \tag{3.25}$$

The solution of this differential equation takes the following form (equation 2.21):

$$x(t) = X_0\, e^{i\omega_n t} \tag{3.26}$$

Of course, in such modal solution, the amplitude X_0 cannot be determined uniquely (CRAIG Jr; KURDILA, 2006; RAO, 2007). Because the software solution was set to be normalized by its maximum modal displacement, however, we know that the set of generalized mass and stiffness used produces unitary maximum displacements, so $X_0 = 1$.

Finally, the the relationship between the modal coordinate and the axial elongation of the piezoelectric patch, at any time t, can be approximated by the linear ratio:

$$x_{patch}(t) = \frac{\Delta L_{patch}}{X_0}\, x(t) = r_p\, x(t) \tag{3.27}$$

Where, in our case, $r_p = 0.0074$.

With this linear relationship, we can correct our model to more strictly incorporate the modal displacement behaviour instead of having some degree of ambiguity as before. First, from the piezoelectric relations (equation 2.58) as seen before:

$$\begin{aligned} Q &= C_p V + \alpha_p (r_p x) \\ F_p &= -\alpha_p V + K_p (r_p x) \end{aligned} \tag{3.28}$$

Those equations, when manipulated into the mechanical and electrical domains just as before, result in the following models for our system (equations 3.1 and 3.3):

$$m\ddot{x} + c\dot{x} + [k + r_p(k_p + \frac{a_p^2}{C_p})]x - \frac{\alpha_p}{C_p} q = f(t) \tag{3.29}$$

$$\alpha_0 \ddot{q} + \alpha_1 \dot{q} + \alpha_2 q + \alpha_{nl} q^3 - \frac{\alpha_p r_p}{C_p} x = 0 \tag{3.30}$$

The use of a generalized form for the model 3.4 allows for an easy update of the transfer functions developed in the sections before, as the same functions (e.g. 3.13, 3.15 or 3.20) can be used but now with their constants changed according to the new model obtained, following from the constants $\alpha_{0,1,2,3,4}$ and $\beta_{0,1,2,3}$.

3.3 Piezoelectric parameters

3.3.1 Theoretical approximation approach

As discussed in chapter 2, the piezoelectric behaviour in bending mode for a thin rectangular patch can be described by the relations 2.58, whose constants depend on its mechanical and piezoelectric parameters. Once which piezoelectric patch should be used in our application has been defined, finding the parameters for the electromechanical model becomes a matter of using its geometric and piezoelectric constants in the equations provided.

The commercial patch considered in this application is the Midé Corporation QP10N (MIDé. . . , , 2020), whose physical properties (obtained from its datasheet) are shown in table 9 below:

Table 9 – PZT-5A physical properties

l (mm)	w (mm)	t (mm)	d_{31} (pm/V)	s_{11} (pm/N)	$\epsilon_{33}^T/\epsilon_0$
45.97	20.57	0.38	−171	16.4	1700

Source: (MIDé. . . , , 2020)

Applying those values to the constants defined by equation 2.58 provides the following approximations for its piezoelectric parameters (Table 10):

Table 10 – Theoretical approximation to the piezoelectric constants

α_p	C_p	k_p
-2.15×10^{-1}	32.94×10^{-9}	10.40×10^{6}

3.3.2 Datasheet approach

A more reliable approach for obtaining the same constants is by the direct use of the data provided for the same patch considered above in its datasheet (Midé Corporation, model QP10N) (MIDé. . . , , 2020). Figure 15 below provides the Force-Voltage-Strain behaviour of the patch in graphical form, alongside the force geometry assumed for the assembly.

Figure 15 – Data sheet information (Midé QP10N)

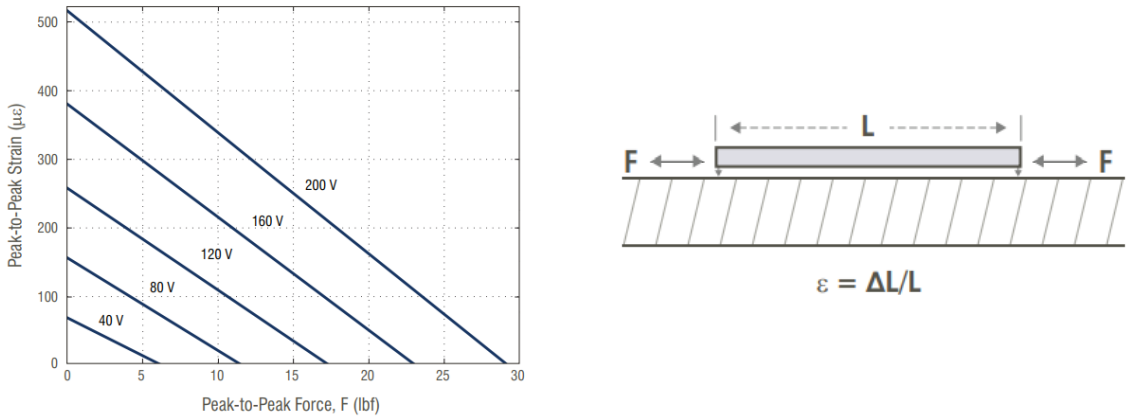

Source: (MIDé. . . , , 2020)

We can infer from the figure above, as expected from equation 2.58, that the Force-Voltage-Strain behaviour of the patch approximately describes a plane. With some of the points - for example the ones crossing the null strain and null force axes - provided in the graph, then, we can find the best fit plane through a quick optimization in Python. To do so, one could make use of the *Optimize* package inside the **SciPy** library, more specifically the *scipy.optimize.minimize* function. Here, however, due to the small data set size and nice invertibility properties of the resulting matrices, an analytical solution approach was used.

The snippet of code below shows how the data points were transitioned into the appropriate dimensions by the use of needed conversion factors and the length of the piezoelectric patch (see figure 15).

```
# Defining variables from the datasheet (approximate values)
```

```
l_piezo = 1.81*0.0254
# F = K_p * x + a_p * V_p
V_values = np.array([40, 40, 80, 80, 120, 120, ...
                     160, 160, 200, 200])
PPS_values = (l_piezo*0.000001)*np.array([70, 0, ...
                     150, 0, 250, 0, 375, 0, 520, 0])
PPF_values = 4.44822*np.array([0, 6, 0, ...
                     11.5, 0, 17, 0, 22.5, 0, 28])
```

Now, considering a multi-variable linear-regression optimization problem of the form:

$$Y = \Theta \cdot X \tag{3.31}$$

Where X and Y are the input and output matrices respectively, it can be shown that its analytical solution for the parameters Θ_{opt} takes the form (GOODFELLOW et al., 2016, c. 5):

$$\Theta_{opt} = (X^T X)^{-1} X^T Y \tag{3.32}$$

The constants of the plane (F_p as a function of voltage and strain) could then be obtained by finding the optimal parameters matrix as below:

```
# Setting up X and Y
X = np.array([PPS_values, V_values]).transpose()
Y = PPF_values
# Find Theta that provides the best fit plane:
Theta_opt = np.linalg.inv(X.transpose().dot(X))
            .dot(X.transpose()).dot(Y)
print(Theta_opt)
```

The resulting parameters obtained give then one of the two equations in 2.58:

$$F_p = (5.62119598E + 06)x + (-6.19987925E - 01)V \tag{3.33}$$

The inherent capacitance was directly obtained from the data sheet, having a value of 55 nF. The constants are finally explicitly laid out in Table 11 below:

As can be seen, although the datasheet and theoretical approximation values for the constants all stay within roughly the same order of magnitude, there are some

Table 11 – PZT-5A patch - resulting constants, equation 2.58

α_p	C_p	k_p
-6.20×10^{-1}	55×10^{-9}	5.62×10^{6}

significant divergences which should lead to different time and frequency damping efficiency results later on. The values obtained from the datasheet will be therefore used as we have reasonable grounds to believe it should be closer to the actual values of the piezoelectric patch.

3.3.3 Experimental approach

Given the appropriate experimental setup for the vibration control problem in question, experimentally obtaining the stiffness and electromechanical coupling factors k_p and α_p (or Θ, as is common to find in the references) is a very uncomplicated and well-documented process in the literature (ERTURK; INMAN, 2008; TANG; YANG, 2012; ZHANG; TANG; LIU, 2017).

It should be noticed that such an approach would allow for a more straightforward use of the electromechanical model obtained by equations 3.3 and 3.1, without the need for the conceptual corrections provided by the r_p factor as presented in the above section, as the overall electromechanical coupling factor Θ measured would positively express the equivalent structure-patch coupling in an inherent manner, already taking into account geometrical and positioning relationships between structure and piezoelectric element (TANG; YANG, 2012; ZHANG; TANG; LIU, 2017), being then the ideal approach for the obtention of any electromechanical constants in general piezoelectric problems such as this one, and definitely the one that would be here used had the experimental and developmental situations allowed.

3.4 Electrical parameters

Equipped with the piezoelectric and mechanical parameters, the need for optimizing the frequency- and time-domain responses of our vibration problem allows for some leeway in the selection of $\alpha_{0,1,2,nl}$ in a broad sense. More specifically, each of these constants will have some bounding constraints limiting the scale of values it can assume for different reasons:

- $\alpha_\mathbf{0}$ is associated with a physical inductance in the shunt circuit, as per its general electric-domain differential equation (SILVA et al., 2018; ZHOU; THOUVEREZ; LENOIR, 2014a). As such, due to the sizeable geometry of inductors intrinsic to high inductances, this constant has an upper bound not greater than 0.1. The range of values assumed for α_0 was [0.01, 0.1].

- $\alpha_{\mathbf{2}}$ should ideally be zero as to eliminate linear-behaviour trends in the damping system and allow for better broadband performance (ZHOU; THOUVEREZ; LENOIR, 2014a), but it can't quite reach nullity due to stability issues (SILVA et al., 2018). It was thus assumed a value in the ballpark of 10^{-9}.

- $\alpha_{\mathbf{1}}$ and $\alpha_{\mathbf{nl}}$ should both fall within the limits of physical reason, what provides a quite ample spectrum of possibilities. To deal with this, first an exponentially increasing range $[10^{-3}, 10^{22}]$ will provide the ballpark of their optimum values, which will then be linearly fine-tuned in the vicinities of the latter.

While the literature has shown several ways to try and optimize the response of our system (through power transfer optmization, for example, as seen in the literature (TANG; YANG, 2012) (TOIT, 2005, p. 65)), here the optimal combination of parameters will be found as to minimize peak frequency response by looping through a range of possible combinations.

To find such optimal combination, a short python script was written as described below. The frequency response was used as the domain by the use of the transfer functions 3.13 and 3.20 and the resulting set of values was compared to guarantee a consistent solution.

3.4.1 Python script for finding the optimal electrical-domain parameters

While the whole script can be found in the appendices, below is a brief description of how the optimal set of values was found for each case; in particular: how the ranges of values were set, how such ranges were swept, how the frequency response was obtained and registered, and how the set which provided the minimal response was identified. As described before, it will be considered the presence of no structural damping at first ($c = 0$) as a critical case, and in the future we can compare the response of the system with approximate considerations for the damping included.

Finding the order of magnitude of $\alpha_{1,nl}$: Here an exponentially spaced range was created through which both values could loop. Because this step produces a smaller set of possible values than later ones, it was appropriate to visually inspect some samples of the frequency response results plots generated by the possible values here obtained, discarding the ones which were physically inappropriate or didn't correspond to the expected frequency response performance.

```
range_a0 = [0.01, 0.025, 0.05, 0.075, 0.1]
range_a1 = []
a2 = 1E-9
range_anl = []
```

```
value = 0.001
i = 0
while i <= 22:
        value *= 10
        range_a1.append(value)
        range_anl.append(value)
        i += 1
```

Fine-tuning $\alpha_{1,nl}$: Once the script was run once and first guesses for $\alpha_{1,nl}$ were acquired, the next iterations would move on to a linearly spaced range of values, where each iteration would have reduced steps and range width around the former values. For example:

```
range_a1 = np.arange(100, 500, 10)
range_anl = np.arange(0.001, 0.05, 0.001)
```

Looping through $\alpha_{1,nl}$: With each range set, every iteration would sweep through the frequency-responses of the transfer functions given the current set of possible values of $\alpha_{1,nl}$ with simple compound loops:

```
for a0 in range_a0:
  for a1 in range_a1:
    for anl in range_anl:
      # Definition of the transfer function
      ...
      # Obtention of the frequency response
      ...
      # Appending peak value to list of results
      ...
```

Obtaining the frequency response: For all of the scripts in this work, both the **NumPy** and **SciPy** libraries (SCIPY..., , 2020) were utilized throughout. For the frequency analysis, the functions *.TransferFunction* (scipy.signal.TransferFunction) and *.bode* (scipy.signal.bode) (SCIPY..., , 2020) of the SciPy Signal Processing library were used. Here, the set of constants for the transfer function is exactly the one provided by equation 3.20, so what we are doing here is optimizing the parameters for the base excitation case. For each iteration, the maximum value of the response obtained was appended to the end of a list of peak values, alongside its generating values of $\alpha_{0,1,nl}$.

```
# Damped system: call system as transfer function
sys = signal.TransferFunction([N5, N4, N3, N2, N1, N0], ...
```

```
                                    [D6, D5, D4, D3, D2, D1, D0])
# Damped system: call bode plot
w, mag, phase = signal.bode(sys, n=3000)

# Define metric for selecting optimal values
max_mag = np.max(mag)

# Expand lists of values
list_a0.append(a0)
list_a1.append(a1)
list_anl.append(anl)
list_mag.append(max_mag)
```

Obtaining the optimal set: Now, getting the optimum values was a matter of sorting the appended lists, after the finish of all the for-loops, according to the lowest peak found in the frequency responses:

```
indices_mag = np.argsort(list_mag)
ptimal_a0_list = [list_a0[index] for index in indices_mag]
optimal_a1_list = [list_a1[index] for index in indices_mag]
optimal_anl_list = [list_anl[index] for index in indices_mag]

# Print optimal values
print(('a0', 'a1', 'anl'), (optimal_a0_list[0], ...
                                optimal_a1_list[0], ...
                                    optimal_anl_list[0]))
```

The algorithm presented was used for the fundamental frequency of the considered single-degree-of-freedom system ($\omega_1 = 124$ Hz, $m_{1,g} = 2.76 \times 10^{-2}$, $k_{1,g} = 1.67 \times 10^{+4}$ N/m), but without the fine-tuning step as our current expectations are to provide a ballpark of the values to be later used experimentally. This resulted in the set of rough values found in table 12 below:

Table 12 – Ballpark of optimal electric parameters obtained

α_0	α_1	α_{nl}
0.05	1×10^3	7×10^{12}

3.5 Frequency-domain response solutions

With the values of all the constants in hand, we can simulate the behaviour of our system to assess its response with and without the piezoelectric NES damping, and, as so,

its effectiveness.

The snippet of code below was used for plotting the response of the base motion case handled above, for both the undamped and NES-damped case.

```
# Damped system: call system as transfer function
sys = signal.TransferFunction([N5, N4, N3, N2, N1, N0], ...
                              [D6, D5, D4, D3, D2, D1, D0])
# Damped system: call bode plot
w, mag, phase = signal.bode(sys, n=3000)

# Undamped system: call system as transfer function
sys2 = signal.TransferFunction([c, k], [m, c, k])
# Undamped system: call bode plot
w2, mag2, phase2 = signal.bode(sys2, n=3000)

# plot optimal values response
    ...
```

As the purpose of using a nonlinear energy sink is precisely to achieve large frequency range damping dynamically, excitation on more than one mode of vibration should be considered, the system being optimized for the fundamental one notwithstanding. This is achieved, as one would expect, by varying the generalized stiffness k_g and mass m_g used on the transfer functions above. Proceeding as so for the first five natural frequencies (Table 3) provides the response observed in figures 16 and 17 below:

Figure 16 – Fundamental frequency response

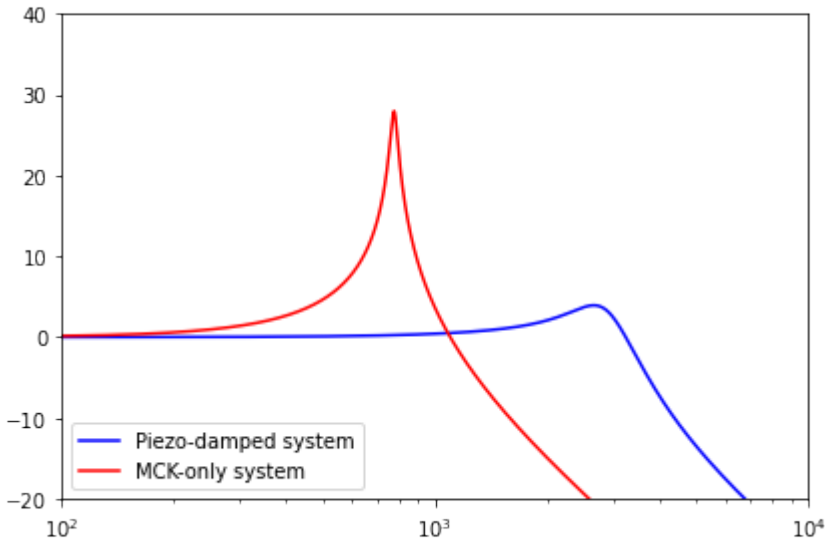

Figure 17 – Second to Fifth natural frequencies response

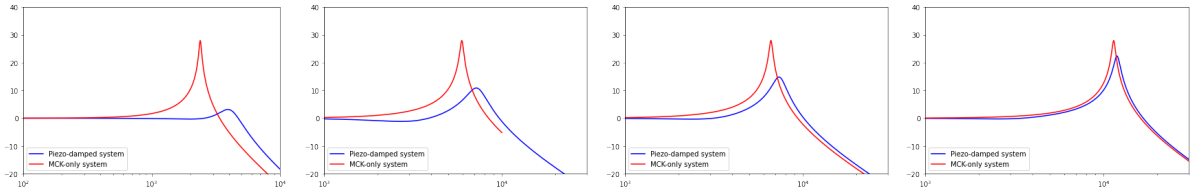

What the graphs above provide us is the comparison between the peak amplification in the modal coordinate response of the system, given a certain frequency of the excitation in the base, with and without the use of our nonlinear energy sink. It's clear that for the first three or four modes the piezoelectric damping action is satisfactory, which could be further demonstrated by plotting the power transfer for the time response of the system, for example. From the fifth mode onwards, however, the damping performance begins to suffer from the mistuned excitation frequency in a trend towards the mode's undamped resonance. A possible workaround could be achieved by tuning the circuit, instead, to higher modes and their natural frequencies (starting from the fourth, for example), which would then provide non-optimal yet acceptable performance for the fundamental mode and extend this acceptable performance to higher modes as well.

3.6 Time-domain response solutions

As a second assessment of the damping performance of the notional nonlinear energy sink proposed, let's concern ourselves with the time response of our system under different circumstances. Evaluating this behaviour would require us to numerically integrate the system of differential equations obtained in the previous sections, more specifically for initial conditions (free response) or forcing cases (base motion).

Fortunately, doing so can be quite straightforward with the **SciPy** library, which provides the *scipy.integrate* package (SCIPY..., , 2020) of which the function *odeint* will be used.

3.6.1 Free response damping performance

Let's first consider the free response of a structurally-damped system provided by our blade. Should the NES system be effective, a quicker vibration speed amplitude decay would be observed through its use, so simulating such a situation might be of interest.

A unitary displacement was considered as the initial condition. Firstly, we set up the constants and initial conditions of our problem. Afterwards, we need to feed the state vector of our system to a function which will be defined as our system, as follows, as well as the function defining the purely mechanical system:

```
# Set up ODEs system solver for the
# piezo-electro-mechanical system
def piezo_mechanical_system(y, t, params_piezomech):
    x, u, q, w = y
    X0, a0, a1, a2, a3, a4, b0, b1, b2, b3 = params_piezomech
    derivs = [u,
              -(1/b0)*(b1*u + b2*x + b3*q),
              w,
              -(1/a0)*(a1*w + a2*q + a3*(q**3) + a4*x)]
    return derivs

# Set up ODEs system solver for the
# purely mechanical system
def mechanical_system(y, t, params_mech):
    x, u = y
    X0, m, c, k = params_mech
    derivs = [u,
              -(1/m)*(c*u + k*x)]
    return derivs
```

With the systems set up, the *odeint* function just needs to be called and from the solution generated each vector of interest plotted accordingly:

```
# Set time array for ODE solver
TimeFinal = 0.1
TimeStep = 0.0001
t = np.arange(0., TimeFinal, TimeStep)

# Call the ODE solvers
Solution_piezomech_xuqw = odeint(piezo_mechanical_system,
            y0_piezomech, t, args=(params_piezomech,))
Solution_mech_xuqw = odeint(mechanical_system,
            y0_mech, t, args=(params_mech,))
```

The results produced from this procedure can be observed in figures 18 and 19 below. Here, again, we can observe that while the decay is indeed faster for the first natural frequencies, the damping performance of our notional system starts dropping from the fourth or fifth natural frequencies as expected, which reflects the behaviour observed previously on the frequency response.

Figure 18 – Free vibration time response, fundamental frequency

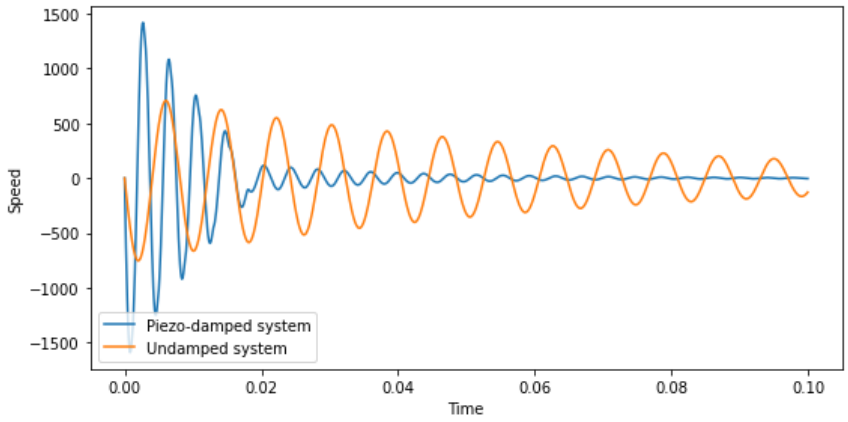

Figure 19 – Free vibration time response, Second to Fifth natural frequencies

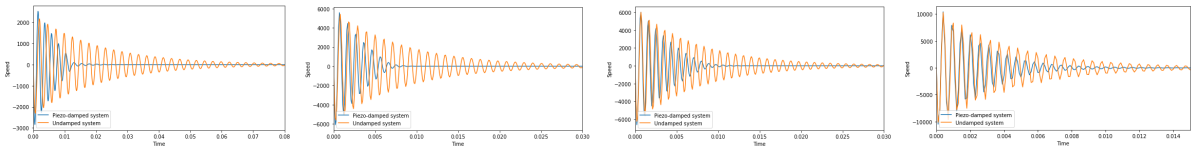

3.6.2 Base motion damping performance

With a basic understanding of the free response damping performance of the NES system, we can now assess the base motion damping performance as it is precisely what the previous frequency response methodologies have dealt with so far. To do so, the same integration procedures can be implemented, but now including zero initial conditions and an harmonic base excitation of the type:

$$x_1 = X_1 sin(\omega_b t)$$
$$\dot{x}_1 = X_1 \omega_b cos(\omega_b t)$$

Where ω_b, the frequency of the base excitation, can of course take arbitrary values but in the case considered will be equal to each mode's natural frequency to study the resonance behaviour of the whole system.

The new system functions to be called now take the following form:

```
# Set up ODEs system solver for the
# piezo-electro-mechanical system
def piezo_mechanical_system(y, t, params_piezomech):
    x, u, q, w = y
    X1, omega, a0, a1, a2, a3, a4, ...
```

```
        b0, b1, b2, b3 = params_piezomech
    derivs = [u,
              -(1/b0)*(b1*(u - X1*omega*np.cos(omega*t)) +
                       b2*(x - X1*np.sin(omega*t)) + b3*q),
              w,
              -(1/a0)*(a1*w + a2*q + a3*q*q*q +
                       a4*(x - X1*np.sin(omega*t)))]
    return derivs

# Set up ODEs system solver for the
# purely mechanical system
def mechanical_system(y, t, params_mech):
    x, u = y
    X1, omega, m, c, k = params_mech
    derivs = [u,
              -(1/m)*(c*(u - X1*omega*np.cos(omega*t)) +
                       k*(x - X1*np.sin(omega*t)))]
    return derivs
```

The position and speed results obtained from the integration of these systems can be seen below in figures 20 and 21:

Figure 20 – Base excitation time response at the fundamental frequency

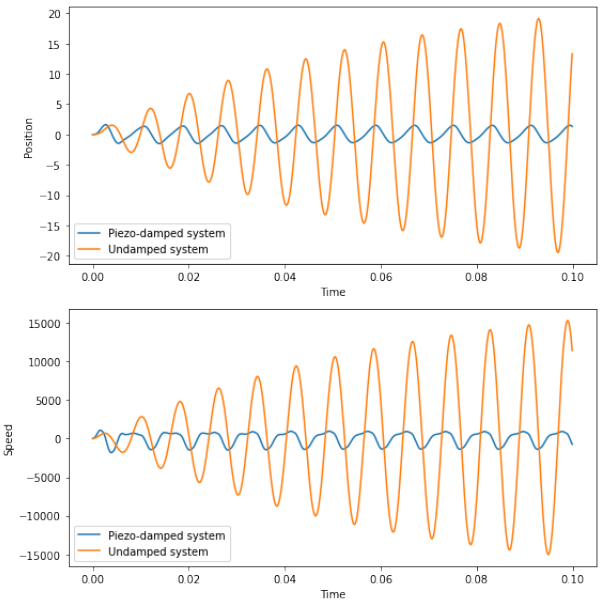

Figure 21 – Base excitation time response, Second to Fifth natural frequencies

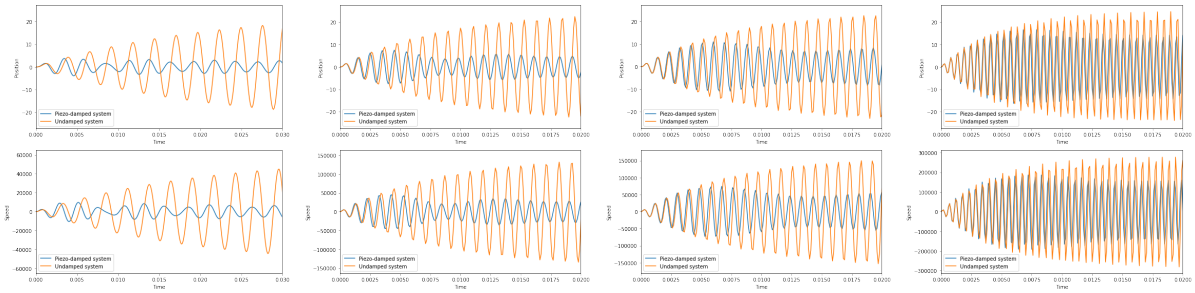

4 CONCLUSION AND FURTHER DEVELOPMENTS

In this work, a notional model of a nonlinear energy sink is proposed as a possible blade vibration control application, and the principles for the mechanical and piezoelectric parameters acquisition are laid out and exemplified for the system (blade and piezoelectric patch) considered. Simplified electromechanical models are established and, from them, the ballpark of resulting electrical parameters (shunt circuit) are obtained with the intent of maximizing attenuation. The final, complete system is assessed on its performance through brief simulations in the frequency and time domains.

With the results obtained from the models and simulations regarding the discussed blade-NES system, we can draw some general conclusions and propose ideas and guidelines for the next steps of this project.

Firstly, a brief discussion will be developed on the numerical results obtained. Afterwards, some suggestions will be laid out regarding future experimental applications for the NES-based vibration control of bladed disks, followed by possible improvements on the modelling techniques used, and finally exploring more precise techniques for the parameters acquisition for simulation, experimental and comparison purposes.

4.1 Conclusions on the simulation results

The notional nonlinear energy sink here modelled and simulated has been proven effective in achieving vibration attenuation, at least theoretically, in more than one natural frequency for the studied blade. It's shown that the addition of the nonlinear energy sink demonstrates great attenuation potential through a range of frequencies when compared to the undamped blade model. It has to be noted, however, that, as expected by the literature, such effect is not perfect throughout all of the first natural frequencies.

Improvements on the aimed tuning frequency (for example by focusing on higher natural frequencies instead of the fundamental one) and on the fine tuning of the electrical parameters in our model could push the broadband attenuation even further. It's interesting to notice, however, that even with limited ranges for general circuit inductance, as considered here, optimization and consequently effective damping can be achieved through higher orders of magnitude in the nonlinear factor, for example, as expected by the literature (SILVA et al., 2018; ZHOU; THOUVEREZ; LENOIR, 2014a), what can generally be dealt with through appropriate selection of electronic (multiplier) elements and can improve compactness for future experimental implementations.

4.2 Proposed improvements and further developments

4.2.1 Development of higher order models for the system

Although a single-degree-of-freedom model is a simple and effective solution for the investigation of the fundamental mode (and other specific natural modes) of the blade, the modelling of both a single blade and a bladed-disk system might require higher order models for the appropriate time domain assessment of its vibration behaviour. By focusing on the blade dynamics instead of the bladed disk, we've ignored some possibly relevant system caveats that should influence blade behaviour on our expected application, as for example through mistuning patterns and their variation, disk-focused modes, and blade-to-blade coupling. A broadband attenuation achieved in the design of future circuits, however, should mitigate the relevance of these influences.

Fortunately, there is no shortage of references from which to draw the appropriate modelling techniques as the subject has been very well documented through past decades. Not only general the theory of vibrations has been thoroughly applied to the study of turbomachinery (RAO, 1991), specific characteristics of such systems can be deeply explored as well.

For example, general structural modelling approaches and the study of mistuning patterns (CASTANIER; PIERRE, 2006; DUAN; ZANG; PETROV, 2016; LIM et al., 2007; ZHOU; THOUVEREZ; LENOIR, 2014a; ZHOU; THOUVEREZ; LENOIR, 2014b) might provide the mathematical groundwork for more precise models and simulations. The literature also provides references for the inclusion of aerodynamic effects (BERTHILLIER et al., 1997; PETROV, 2010; PETROV et al., 2010) and blade coupling effects (AVALOS; MIGNOLET, 2010) for more complete models.

When dealing with FEA/FEM blade models specifically, the basis for element selection (BROWN, 1997) and general modal analysis procedures (INOYAMA, 2003) can be helpful. More complete systems, such as the assembly of several bladed disks (GRIFFIN, 1988; SLATER; MINKIEWICZ; BLAIR, 1999; STERNCHÜSS, 2009; STERNCHÜSS et al., 2009) and rotor assemblies (BAB et al., 2017) can expand on the model when dealing with complex structures.

Finally, several piezoelectric applications for the control of bladed disk have been developed in the recent past (KAUFFMAN; LESIEUTRE, 2012; YU; WANG, 2007; YU; WANG, 2009; ZHOU; THOUVEREZ; LENOIR, 2014a; ZHOU; THOUVEREZ; LENOIR, 2014b) and the use of other damping methods and joint friction studies (CHARLEUX et al., 2006; JAISWAL; BHAVE, 1994; KRACK MALTE; THOUVEREZ, 2017; LAXALDE DENIS; LOMBARD, 2007; PETROV; EWINS, 2006; PETROV; EWINS, 2007; TEHRANI; DARDEL, 2019) can provide a broader scope for vibration control applications.

4.2.2 Future experimental procedures

As explained in the beginning of this document, the logical continuity for this study should include a few next steps, which could have been the focus of this work under more favourable circumstances. The purpose of this section is not to precisely define how such implementations should be developed and by which approach, but rather to enumerate future challenges in this application, and how they might be of relevance, laying the groundwork for future technical developments.

To such an extent, we can ponder the following:

- **Circuit design:** The appropriate electronic design and optimization of the nonlinear circuit to be used with the piezoelectric patch is of paramount importance for the effectiveness of our system. As seen before, four main elements should constitute this circuit: an inductance, a resistance, a capacitance and a nonlinear element. From the examples in the literature, the last two are not as straightforwardly attained, being achieved through an op-amp-based negative capacitance subcircuit and an op-amp- and multiplier-based nonlinear subcircuit, respectively (SILVA et al., 2018), for example. Once the circuit parameters are fittingly tuned to the blade or blade-disk dynamics, and the electrical-domain model is converted to a physical model, the circuit can be assembled into a printed circuit board, for example, to achieve better assembly capabilities, taking into account circuit installation procedures and power supply demands from the start.

- **Feasibility study:** The study of the physical feasibility of applying the proposed nonlinear energy sink on the vibration attenuation for both a single blade and the bladed disk system as a whole should then be performed, taking into consideration the geometric constraints and compactness needs of the operating environment, the rotor balancing (or resulting unbalancing) and added weight constraints, the available assembly methods, the feasibility of the power needs previously modelled, and the aerodynamic influence of the piezoelectric patch and its positioning. Precisely, some of the biggest challenges regarding future experimental solutions might be related to the bladed disk environment itself, and how the NES system (including its piezoelectric patch, shunt circuit and printed circuit board, wiring and harness, power supply, etc) fits into its operating scheme.

- **Parameter acquisition:** The experimental acquisition (and comparison to the present theoretical values) of the mechanical and piezoelectric parameters for our model should take place o achieve more reliable models and numerical results and to draw comparisons between predicted and actual parameters. For the mechanical parameters, this can be done through the use of experimental modal analysis (SILVA, 2007) and techniques as laid out in section 2 for both the blade and bladed disk -

including the experimental obtention of natural frequencies and vibration modes, modal masses and stiffnesses, and mode-specific or generalized damping ratios. For the piezoelectric parameters, as explained in section 3, there are several established experimental techniques that can be followed as well. Also, the development here presented does not compare the proposed system to any other vibration dampers of any nature (passive, active or hybrid), what can be achieved both theoretically and experimentally once such parameters are reliably acquired.

- **Experimental vibration control:** Finally, the development should proceed to the experimental application of the vibration control system itself, both for the blade in the appropriate testbeds and for the bladed-disk system in its operating environment. At this stage, more practical needs regarding the design, installation and setup of the solution will arise, for example with the definition of the piezoelectric patch location, number of elements and blades to be controlled, among others.

BIBLIOGRAPHY

AMERICANPIEZO'S "What is PZT?". <https://www.americanpiezo.com/piezo-theory/pzt.html>. Accessed: 2020-11-18.

ÅSTRÖM, K. J.; MURRAY, R. M. **Feedback systems: an introduction for scientists and engineers**. [S.l.]: Princeton university press, 2010.

AVALOS, J.; MIGNOLET, M. P. On damping entire bladed disks through dampers on only a few blades. **Journal of engineering for gas turbines and power**, American Society of Mechanical Engineers Digital Collection, v. 132, n. 9, 2010.

BAB, S. et al. Vibration attenuation of a continuous rotor-blisk-journal bearing system employing smooth nonlinear energy sinks. **Mechanical Systems and Signal Processing**, Elsevier, v. 84, p. 128–157, 2017.

BERTHILLIER, M. et al. A numerical method for the prediction of bladed disk forced response. 1997.

BROWN, J. Characterization of msc/nastran & msc/abaqus elements for turbine engine blade frequency analysis. In: CITESEER. **Proc. MSC Aerospace Users' Conference**. [S.l.], 1997.

CASTANIER, M. P.; PIERRE, C. Modeling and analysis of mistuned bladed disk vibration: current status and emerging directions. **Journal of Propulsion and power**, v. 22, n. 2, p. 384–396, 2006.

CHARLEUX, D. et al. Numerical and experimental study of friction damping blade attachments of rotating bladed disks. **International Journal of Rotating Machinery**, Hindawi, v. 2006, 2006.

CORR, L. R.; CLARK, W. W. Comparison of low-frequency piezoelectric switching shunt techniques for structural damping. **Smart materials and Structures**, IOP Publishing, v. 11, n. 3, p. 370, 2002.

CRAIG Jr, R. R.; KURDILA, A. J. **Fundamentals of structural dynamics**. [S.l.]: John Wiley & Sons, 2006.

DUAN, Y.; ZANG, C.; PETROV, E. Forced response analysis of high-mode vibrations for mistuned bladed disks with effective reduced-order models. **Journal of Engineering for Gas Turbines and Power**, American Society of Mechanical Engineers Digital Collection, v. 138, n. 11, 2016.

ERTURK, A.; INMAN, D. J. Issues in mathematical modeling of piezoelectric energy harvesters. **Smart Materials and Structures**, IOP Publishing, v. 17, n. 6, p. 065016, 2008.

_____. **Piezoelectric energy harvesting**. [S.l.]: John Wiley & Sons, 2011.

GENDELMAN, O. et al. Energy pumping in nonlinear mechanical oscillators: part i—dynamics of the underlying hamiltonian systems. **J. Appl. Mech.**, v. 68, n. 1, p. 34–41, 2001.

GENDELMAN, O.; STAROSVETSKY, Y.; FELDMAN, M. Attractors of harmonically forced linear oscillator with attached nonlinear energy sink i: description of response regimes. **Nonlinear Dynamics**, Springer, v. 51, n. 1-2, p. 31–46, 2008.

GENDELMAN, O. V. Transition of energy to a nonlinear localized mode in a highly asymmetric system of two oscillators. **Nonlinear dynamics**, Springer, v. 25, n. 1-3, p. 237–253, 2001.

GOLUB, G. H.; LOAN, C. F. V. Matrix computations, 4th. **Johns Hopkins**, 2013.

GOODFELLOW, I. et al. **Deep learning**. [S.l.]: MIT press Cambridge, 2016. v. 1.

GRIFFIN, J. On predicting the resonant response of bladed disk assemblies. 1988.

GRIPP, J.; RADE, D. Vibration and noise control using shunted piezoelectric transducers: A review. **Mechanical Systems and Signal Processing**, Elsevier, v. 112, p. 359–383, 2018.

INOYAMA, D. Vibration analysis of a fan/compressor blade. 2003.

INSTITUTE OF ELECTRICAL AND ELECTRONICS ENGINEERS, A. S. .-. **IEEE standard on piezoelectricity**. [S.l.]: IEEE New York, 1987.

JAISWAL, B. L.; BHAVE, S. K. Experimental evaluation of damping in a bladed disk model. **Journal of sound and vibration**, p. 111–120, 1994.

JALILI, N. **Piezoelectric-based vibration control: from macro to micro/nano scale systems**. [S.l.]: Springer Science & Business Media, 2009.

JOOS, G.; FREEMAN, I. M. **Theoretical physics**. [S.l.]: Courier Corporation, 2013.

KANG, Y. K. et al. Optimum placement of piezoelectric sensor/actuator for vibration control of laminated beams. **AIAA journal**, v. 34, n. 9, p. 1921–1926, 1996.

KAUFFMAN, J. L.; LESIEUTRE, G. A. Piezoelectric-based vibration reduction of turbomachinery bladed disks via resonance frequency detuning. **AIAA journal**, v. 50, n. 5, p. 1137–1144, 2012.

KRACK MALTE, L. S.; THOUVEREZ, F. Vibration prediction of bladed disks coupled by friction joints. **Archives of Computational Methods in Engineering**, p. 589–636, 2017.

LANDAU, L. D.; LIFSHITZ, E. M. **Course of theoretical physics**. [S.l.]: Elsevier, 2013. v. 1.

_____. **Course of theoretical physics**. [S.l.]: Elsevier, 2013. v. 7.

_____. **Course of theoretical physics**. [S.l.]: Elsevier, 2013. v. 8.

LAXALDE DENIS, F. T.; LOMBARD, J.-P. Vibration control for integrally bladed disks using friction ring dampers. **ASME turbo expo 2007: power for land, sea, and air. American Society of Mechanical Engineers Digital Collection**, 2007.

LIM, S.-H. et al. Compact, generalized component mode mistuning representation for modeling bladed disk vibration. **AIAA journal**, v. 45, n. 9, p. 2285–2298, 2007.

LU, F.; LEE, H.; LIM, S. Modeling and analysis of micro piezoelectric power generators for micro-electromechanical-systems applications. **Smart materials and structures**, IOP Publishing, v. 13, n. 1, p. 57, 2003.

MIDé Corp. QP10N Datasheet. <https://br.mouser.com/datasheet/2/606/QuickPack-actuator-sensor-datasheet-220082.pdf>. Accessed: 2020-11-18.

MSC-PATRAN reference manual. <https://simcompanion.mscsoftware.com/infocenter/index?page=content&id=DOC9284>. Accessed: 2020-11-18.

PETROV, E. A method for forced response analysis of mistuned bladed disks with aerodynamic effects included. **Journal of Engineering for Gas Turbines and Power**, American Society of Mechanical Engineers Digital Collection, v. 132, n. 6, 2010.

PETROV, E.; EWINS, D. Effects of damping and varying contact area at blade-disk joints in forced response analysis of bladed disk assemblies. 2006.

_____. Advanced modeling of underplatform friction dampers for analysis of bladed disk vibration. 2007.

PETROV, E. et al. Forced response of mistuned bladed disks in gas flow: A comparative study of predictions and full-scale experimental results. **Journal of Engineering for Gas Turbines and Power**, American Society of Mechanical Engineers Digital Collection, v. 132, n. 5, 2010.

RAO, J. **Turbomachine blade vibration**. [S.l.]: New Age International, 1991.

RAO, S. S. **Vibration of continuous systems**. [S.l.]: Wiley Online Library, 2007. v. 464.

_____. **Mechanical vibrations**. [S.l.]: Pearson, 2017.

SAFAEI, M.; SODANO, H. A.; ANTON, S. R. A review of energy harvesting using piezoelectric materials: state-of-the-art a decade later (2008–2018). **Smart Materials and Structures**, IOP Publishing, v. 28, n. 11, p. 113001, 2019.

SCIPY 1.5.3 Library Documentation. <https://docs.scipy.org/doc/scipy/reference/>. Accessed: 2020-11-18.

SILVA, C. W. D. **Vibration monitoring, testing, and instrumentation**. [S.l.]: CRC Press, 2007.

SILVA, T. M. et al. An experimentally validated piezoelectric nonlinear energy sink for wideband vibration attenuation. **Journal of Sound and Vibration**, Elsevier, v. 437, p. 68–78, 2018.

SLATER, J.; MINKIEWICZ, G.; BLAIR, A. Forced response of bladed disk assemblies-a survey. In: **34th AIAA/ASME/SAE/ASEE Joint Propulsion Conference and Exhibit**. [S.l.: s.n.], 1999. p. 3743.

STAROSVETSKY, Y.; GENDELMAN, O. Attractors of harmonically forced linear oscillator with attached nonlinear energy sink. ii: Optimization of a nonlinear vibration absorber. **Nonlinear Dynamics**, Springer, v. 51, n. 1-2, p. 47, 2008.

_____. Vibration absorption in systems with a nonlinear energy sink: nonlinear damping. **Journal of Sound and Vibration**, Elsevier, v. 324, n. 3-5, p. 916–939, 2009.

STERNCHÜSS, A. **Multi-level parametric reduced models of rotating bladed disk assemblies**. 2009. Tese (Doutorado) — Châtenay-Malabry, Ecole centrale de Paris, 2009.

STERNCHÜSS, A. et al. Reduction of multistage disk models: application to an industrial rotor. **Journal of Engineering for Gas Turbines and Power**, American Society of Mechanical Engineers Digital Collection, v. 131, n. 1, 2009.

TANG, L.; YANG, Y. A nonlinear piezoelectric energy harvester with magnetic oscillator. **Applied Physics Letters**, American Institute of Physics, v. 101, n. 9, p. 094102, 2012.

TEHRANI, G. G.; DARDEL, M. Vibration mitigation of a flexible bladed rotor dynamic system with passive dynamic absorbers. **Communications in Nonlinear Science and Numerical Simulation**, p. 1–30, 2019.

TIMOSHENKO, S. P.; GOODIER, J. Theory of elasticity. 2011.

TOIT, N. E. D. **Modeling and design of a MEMS piezoelectric vibration energy harvester**. 2005. Tese (Doutorado) — Massachusetts Institute of Technology, 2005.

TRIPLETT, A.; QUINN, D. D. The effect of non-linear piezoelectric coupling on vibration-based energy harvesting. **Journal of intelligent material systems and structures**, Sage Publications Sage UK: London, England, v. 20, n. 16, p. 1959–1967, 2009.

VAKAKIS, A. F.; GENDELMAN, O. Energy pumping in nonlinear mechanical oscillators: part ii—resonance capture. **J. Appl. Mech.**, v. 68, n. 1, p. 42–48, 2001.

VIGUIÉ, R.; KERSCHEN, G.; RUZZENE, M. Exploration of nonlinear shunting strategies as effective vibration absorbers. In: INTERNATIONAL SOCIETY FOR OPTICS AND PHOTONICS. **Active and Passive Smart Structures and Integrated Systems 2009**. [S.l.], 2009. v. 7288, p. 72882B.

YU, H.; WANG, K. Piezoelectric networks for vibration suppression of mistuned bladed disks. 2007.

_____. Vibration suppression of mistuned coupled-blade-disk systems using piezoelectric circuitry network. **Journal of Vibration and Acoustics**, American Society of Mechanical Engineers Digital Collection, v. 131, n. 2, 2009.

ZHANG, Y.; TANG, L.; LIU, K. Piezoelectric energy harvesting with a nonlinear energy sink. **Journal of Intelligent Material Systems and Structures**, Sage Publications Sage UK: London, England, v. 28, n. 3, p. 307–322, 2017.

ZHOU, B.; THOUVEREZ, F.; LENOIR, D. Essentially nonlinear piezoelectric shunt circuits applied to mistuned bladed disks. **Journal of Sound and Vibration**, Elsevier, v. 333, n. 9, p. 2520–2542, 2014.

_____. Vibration reduction of mistuned bladed disks by passive piezoelectric shunt damping techniques. **AIAA journal**, American Institute of Aeronautics and Astronautics, v. 52, n. 6, p. 1194–1206, 2014.